CRATERING STUDIES: LUNAR SURFACE MATERIALS

PIFR-118

May 1969

by

D. W. Baum

Prepared for

NASA
Manned Spacecraft Center
Houston, Texas 77058

Attn: R. G. Cour-Palais/TG2

for Contract NAS9-8031

PHYSICS INTERNATIONAL COMPANY

3.14159265358 97

2700 Merced St., San Leandro, Calif. 415/357-4610

NASA CR 99665

CRATERING STUDIES: LUNAR SURFACE MATERIALS
PIFR-118

May 1969

by
D. W. Baum

Prepared for
NASA
Manned Spacecraft Center
Houston, Texas 77058
Attn: R. G. Cour-Palais/TG2
for Contract NAS9-8031

Physics International Company
2700 Merced Street
San Leandro, California 94577

ABSTRACT

The goal of this research program is the correlation of lunar surface craters with the dynamic properties of impacting meteoroids. Experimental verification of cratering models for possible lunar surface configurations is a prerequisite. An analytic model suitable for describing spherical wave propagation in competent basalt was developed. The model was adjusted to reproduce stress profiles observed in a series of one-dimensional spherical wave experiments in large basalt blocks. The spherical waves were produced by a spherical explosive charge and monitored by piezoresistive manganin gauges. In addition, hypervelocity impact tests were conducted in which 1-g spheres were launched to 6.4 km/sec and impacted against instrumented basalt targets. Stress profiles were obtained at several depths in the target material and final crater measurements were made. Final crater dimensions also were obtained from an 11.6 km/sec impact of a 1.6-g projectile against a basalt slab. The volumes of the craters are compared as a function of projectile energy with previous basalt cratering data.

CONTENTS

ILLUSTRATIONS

ILLUSTRATIONS (cont.)

SECTION I

BACKGROUND

Knowledge of the lunar surface has increased greatly during the last few years as a result of data obtained from the Ranger, Surveyor, Lunar Orbiter, and, most recently, Apollo missions. The Surveyor series gathered direct data concerning the physical and chemical properties of the lunar surface, while the Ranger, Lunar Orbiter, and Apollo series provided close-up photographic evidence of the various sizes and forms of lunar craters. The geometry of the smallest craters visible in the photographs from the Ranger missions, together with laboratory impact tests, led to the interpretation that the lunar surface was composed of loose or very low cohesive strength materials (Reference 1). The Surveyor 5 and 6 missions performed α-particle backscattering experiments, indicating that the lunar surface is basaltic in composition (References 2 and 3). Lunar Orbiter I photographs revealed a distinct correlation between crater size and crater morphology. Subsequent laboratory impact experiments by Oberbeck and Quaide (Reference 4) showed that all of the morphologic classes recognized in the photographs can be produced by impact into a stratified media consisting of a fragmental surface layer overlying a cohesive substrate. They found the most significant parameter in determing the type of crater formation is R, the ratio of crater diameter to surface layer thickness. Assuming that the parameter R has the same relationship to the structure of the lunar craters, the median surface layer thickness surrounding individual craters has been estimated from Orbiter 1, 2, and 3 photographs to vary locally between 4 and 9 meters (References 4 and 5).

Having estimated the physical and chemical properties of the lunar surface and established the impact origin of many lunar craters, the moon provides a ready source of meteoroid impact cratering data. The lack of lunar atmosphere allows meteoroids to impact the surface free from the influence of the complex aerothermochemical effects that accompany terrestrial meteors. A study of lunar craters should then yield information as to the dynamics (energy, velocity), as well as the flux and frequency distribution of impacting meteoroids.

SECTION II

INTRODUCTION

For the past 11 months Physics International Company has been engaged in an experimental-analytical program for the National Aeronautics and Space Administration, Contract No. NAS 9-8031, to correlate the size and morphology of lunar surface craters with the mass and velocity of an impacting meteoroid. The first milestone toward attaining this goal is to analytically simulate a hypervelocity impact crater in competent basalt. Basalt was chosen for this initial study because of its similarity in chemical composition to the lunar surface layer as determined by Surveyor 5 and 6 (References 2 and 3). The work performed in the present phase of the program consisted of a series of hypervelocity impact tests, as well as the experimental and analytical efforts necessary to define a cratering model for basalt. The rock samples used throughout this program were obtained from the Basalt Rock Company, Napa, California.

A series of dynamic and static experiments was performed in the basalt modeling phase of the program. The static tests measured the density, porosity, and zero-pressure longitudinal and shear wave velocities of the basalt samples. Dynamic tests utilized in-contact explosives and were carried out in both plane and spherical geometries, the latter being the most appropriate to cratering experiments. Extensive use was made of manganin gauges in measuring peak stress attenuation rates and stress profiles as a function of thickness of basalt traversed. Because of the existence of high-pressure data for Vacaville basalt, the present tests were limited to low pressures ($<$ 100 kbar). The combined data from all tests were incorporated with a proposed material response model in an iterative computational procedure using POD, Physics International's one-dimensional, time-dependent, elastic-plastic Lagrangian computer code to reproduce the stress behavior observed in the dynamic tests. The resulting analytic model should then represent a best fit to the existing data.

The hypervelocity launchers used in this program were designed and developed at Physics International Company before this program began (References 6 to 8). The basic device launches a saboted 1-g magnesium-lithium alloy (LA141A) sphere to a 6.4 km/sec impact velocity. A single-stage fast gun of recent design was used to launch a 2-g, right-circular cylinder to an impact velocity of 11.6 km/sec. The basalt targets for these shots were instrumented with embedded piezoresistive manganin gauges to measure stress-time profiles and/or a pulsed radiograph unit to observe material ejected during crater formation. For one shot at 6.4 km/sec and one shot at 11.6 km/sec, a large target assembly was designed to permit terminal observation of the resulting craters without perturbing edge effects.

This report details the work described above, including pertinent data and the resulting analytic model.

SECTION III

BASALT MODELING EXPERIMENTS

A. DYNAMIC ONE-DIMENSIONAL STRAIN

The initial response of materials to shock waves generated by impact cratering can be treated by a hydrodynamic description. It is assumed that when the stresses are sufficiently large, the constitutive properties of the materials are relatively unimportant. In the late stages of crater formation, however, the stresses are small and material strength cannot be neglected. Particularly in brittle materials, the final crater size is very dependent on material strength, as evidenced by the large volume of basalt craters compared to those formed by similar impacts in aluminum.

Existing Hugoniot data for basalt as reported by Gregson, et al., at Stanford Research Institute (Reference 9) and Jones et al., at General Motors (Reference 10) extend from stress levels of 100 kbar to 2.0 Mbar. A two-wave structure was observed by Gregson, et al., the magnitude of the precursor being approximately 50 kbar. The experiments were performed in a plane wave geometry and diagnosed through optical techniques. The General Motors data, on the other hand, were obtained in plane-wave geometry using a pin technique to record shock arrival times. The GM Hugoniot data for Vacaville basalt were plotted along with data from other basalts of differing density (Reference 10). The Hugoniot curves for the various basalts coincided to within the experimental accuracy of the data. Thus it was assumed that even though the present basalt samples were not obtained from Putnam Peak (near Napa, California) as were the samples studied by Gregson and Jones, the reported Hugoniot data were applicable to our basalt. One plane-wave shot was fired in the present program to confirm the usefulness of the existing data. A P-40 plane wave lens was used to drive a shock into a 1.27-cm-thick Plexiglas attenuator plate adjoining a 2.54-cm-thick basalt specimen. Instrumented with manganin gauges, the stress amplitude and arrival times at different locations were monitored, allowing the calculation of shock and particle velocities. The resulting Hugoniot point of 75 kbar agreed with the existing data (References 9 and 10) to within experimental accuracy.

Emphasis in the present program was on determining a model capable of describing the behavior of basalt in the low stress regime. The model should join smoothly with existing Hugoniot data. A technique was used whereby spherical shock waves in the low stress range were produced. Instrumented with manganin gauges, stress-time profiles at various radii were observed. Then using computer analysis a material model was developed that was capable of describing the observed response. The spherical geometry chosen for the modeling experiments has several advantages: (1) the divergent geometry is similar to that occurring in cratering processes, (2) the samples can be made sufficiently large that the response is not dominated by small-scale inhomogeneities, and (3) large amounts of data can be collected from a single experiment.

The blocks of basalt were prepared as shown in Figure 1. The maximum size of these blocks was approximately one cubic foot. The size of the block and placement of the high explosive in the block was selected so that reflections from a free surface could not reach any of the stress gauges during the time of observation. This limited the range of radii that could be observed on any one shot.

To prepare a block for testing, a cylinder of the sample material is removed by drilling with a diamond-tipped core drill, and a hemisphere is lapped at the bottom of this cylindrical hole. A sphere of

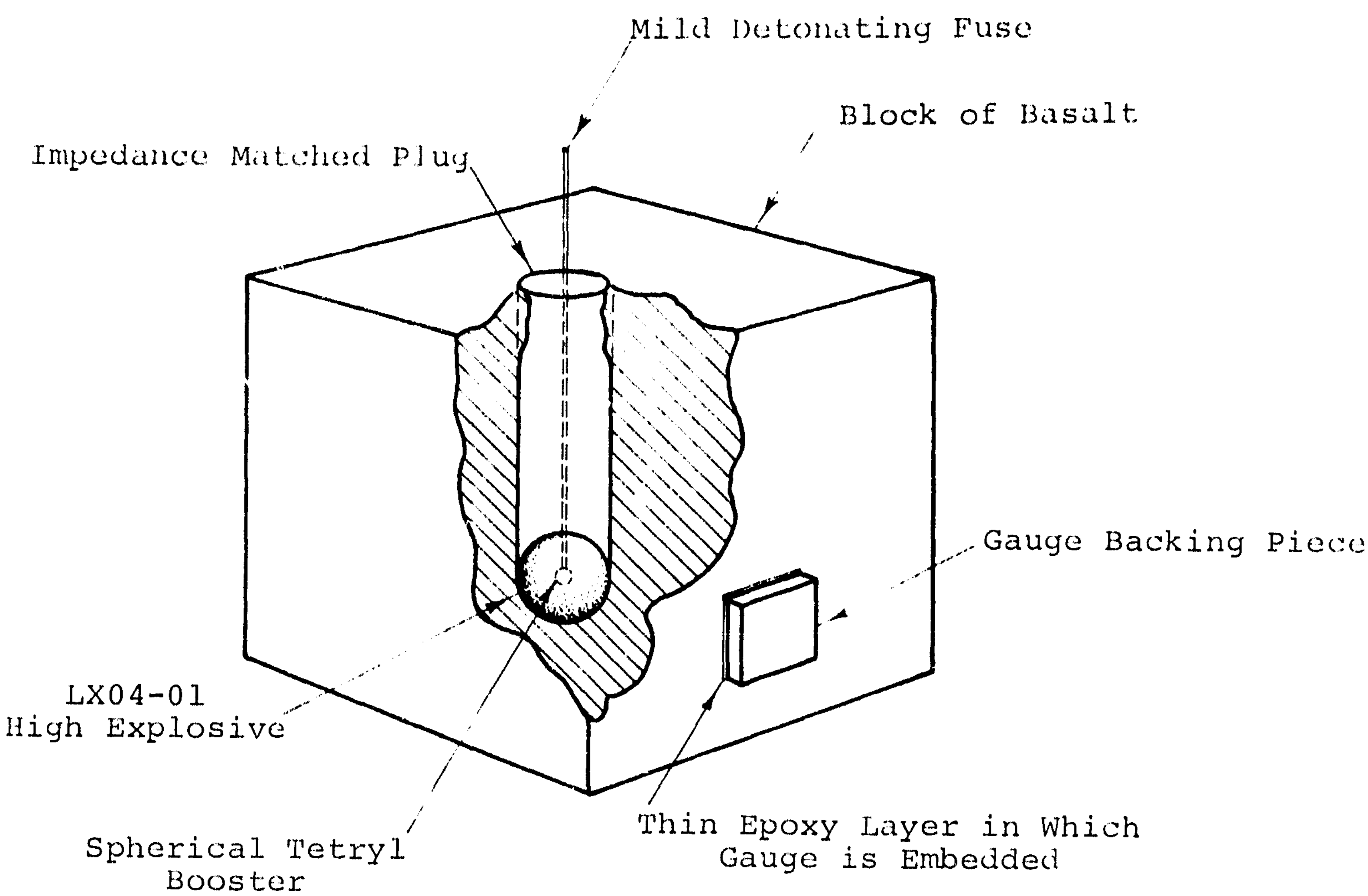

FIGURE 1. BASIC EXPERIMENTAL CONFIGURATION FOR MODELING TESTS

high explosive (LX04-01) is placed in the hemisphere. The explosive sphere contains a spherical tetryl booster at its center, which in turn is detonated by a mild detonating fuse (MDF) at its center. The equation of state of the explosive has been thoroughly studied (Reference 11), and its Chapman-Jouquet pressure has been measured as 360 kbar. The hole is filled with a cylindrical aluminum plug (aluminum provides an impedance match with basalt and is easily machined) shaped to fit the top half of the explosive sphere. The MDF is brought out through a small hole in the center of the plug.

With the explosive charge placed asymmetrically, the five remaining faces of the block were at different radii. Manganin stress gauges were placed on the faces opposite the high explosive, and the spherical stress wave produced by the ensuing detonation was monitored at five different radii.

The manganin gauge was developed by Bernstein and coworkers (References 12 and 13) and has been calibrated for stresses up to 290 kbar. The calibration factor relates the percent change in resistance of manganin to the magnitude of the applied stress. When supplied by constant current, the ideal relative voltage change resulting from shock passage is linearly related to the stress amplitude associated with the shock. The stress is determined as follows: the relative change in voltage is simply the ratio of the voltage variation resulting from the shock (ΔV) to the dc voltage (V_o). The voltage change in percent is related to the stress (P) by the relations,

$$\frac{\Delta V}{V_o} (\%) = 0.29 P \quad \text{for } 0 < P < 150 \text{ kbar}$$

$$\frac{\Delta V}{V_o} (\%) = 16 + 0.18 P \quad \text{for } 150 < P < 290 \text{ kbar}$$

The particular gauge design for this program consisted of a single strand of 3-mil-diam manganin wire supplied by a constant current power source. Two 3-mil signal leads were spot-welded to the current-carrying manganin wire to monitor the voltage across a 7 mm segment of the wire (see Figure 2). The voltage variations were fed through a differential preamplifier and monitored on an oscilloscope. The complete gauge and lead wire assembly was embedded in a thin layer of epoxy and backed by a small slab of basalt. The total thickness of the epoxy layer with the embedded manganin gauge was less than 0.25 mm. The lateral extent and depth of the basalt backing pieces was large enough so that reflected waves from the edges were unable to reach the gauges for at least 4 μsec after the shock passage. The time required for the manganin gauge and epoxy layer to equilibrate with the rock has been calculated to be 0.1 μsec (Reference 14). Because the resolution obtainable from the manganin gauge records was roughly 0.2 μsec, the observed stress profiles were not corrected for gauge equilibration time.

An additional contribution to the output voltage of the manganin gauge is significant for nonplanar stress pulses. The divergence associated with the material displacement behind spherical and cylindrical waves causes the manganin wire to stretch. Assuming a constant resistivity the resistance of the wire changes because the diameter decreases and the length increases as the wire stretches. This change is seen as an output voltage and must be subtracted from the apparent stress profile as taken directly from the oscilloscope record. This effect is increasingly important for measurements some distance behind the front of the stress pulse. The stretching signal can be measured by using a copper-nickel wire as a gauge element that responds only to dimensional changes and is not piezoresistive. A loop was formed (as shown in Figure 2) consisting of one wire of manganin and one of a copper-nickel alloy having nearly the same resistivity and

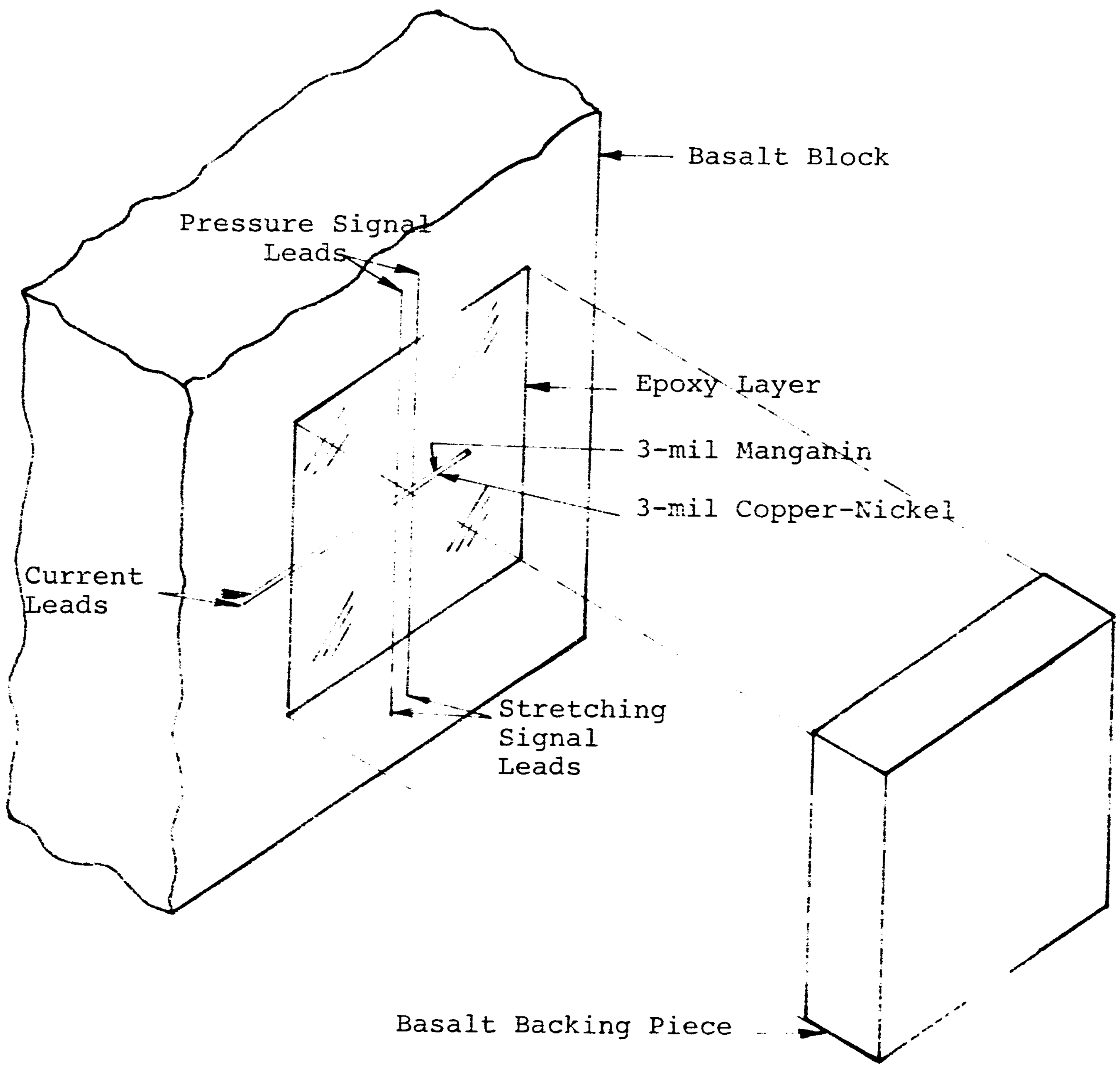

FIGURE 2. DETAIL OF GAUGE CONSTRUCTION

mechanical properties. Supplied by a constant current power supply, the voltage across a 7-mm segment of each wire was monitored on an oscilloscope. The output signal from the manganin gauge is related to the pressure in the epoxy layer as well as the stretching of the wire, while the voltage change across the copper-nickel wire is due entirely to stretching. Therefore, subtracting this signal from the manganin signal, eliminates the stretching effect. The mangnitude of this correction is typically a few percent, and in some case negligible. An alternative procedure for correcting the manganin gauge signal, used when the copper-nickel signal was lost, involved calculating a correction factor. Although the calculation is necessarily approximate, it provides a reasonable correction to within the experimental accuracy of the manganin gauge signal.

Three spherical block tests were fired with basalt samples. Shots 395-2 and 395-4 utilized explosive spheres with a radius, R_o, of 2.54 cm. Stress-time profiles obtained from these shots at scaled radii, R/R_o, ranging from 1.585 to 4.50, are shown in Figure 3. The profiles have been corrected for stretching but not for gauge equilibration. The shock front is seen to undergo little dispersion, which is indicative of a fine-grained, homogeneous material. There is no evidence on the time scale in Figure 3 of a two-wave structure, although the raw data for the smallest radius had a slight knee at the 52.4-kbar stress level. Because a similar perturbation was not observed at larger radii, no significance was ascribed to the knee.

The measured peak radial stresses from Shots 395-2, 395-3, and 395-4 are plotted as a function of scaled radius in Figure 4. Shot 395-3 was a twice-scale version of 395-2, having a 5.08-cm cavity radius. The peak stresses are seen to attenuate at the same rate for both the 2.54- and 5.08-cm cavity radius tests, indicating that time-dependent effects have a negligible influence on the peak stress

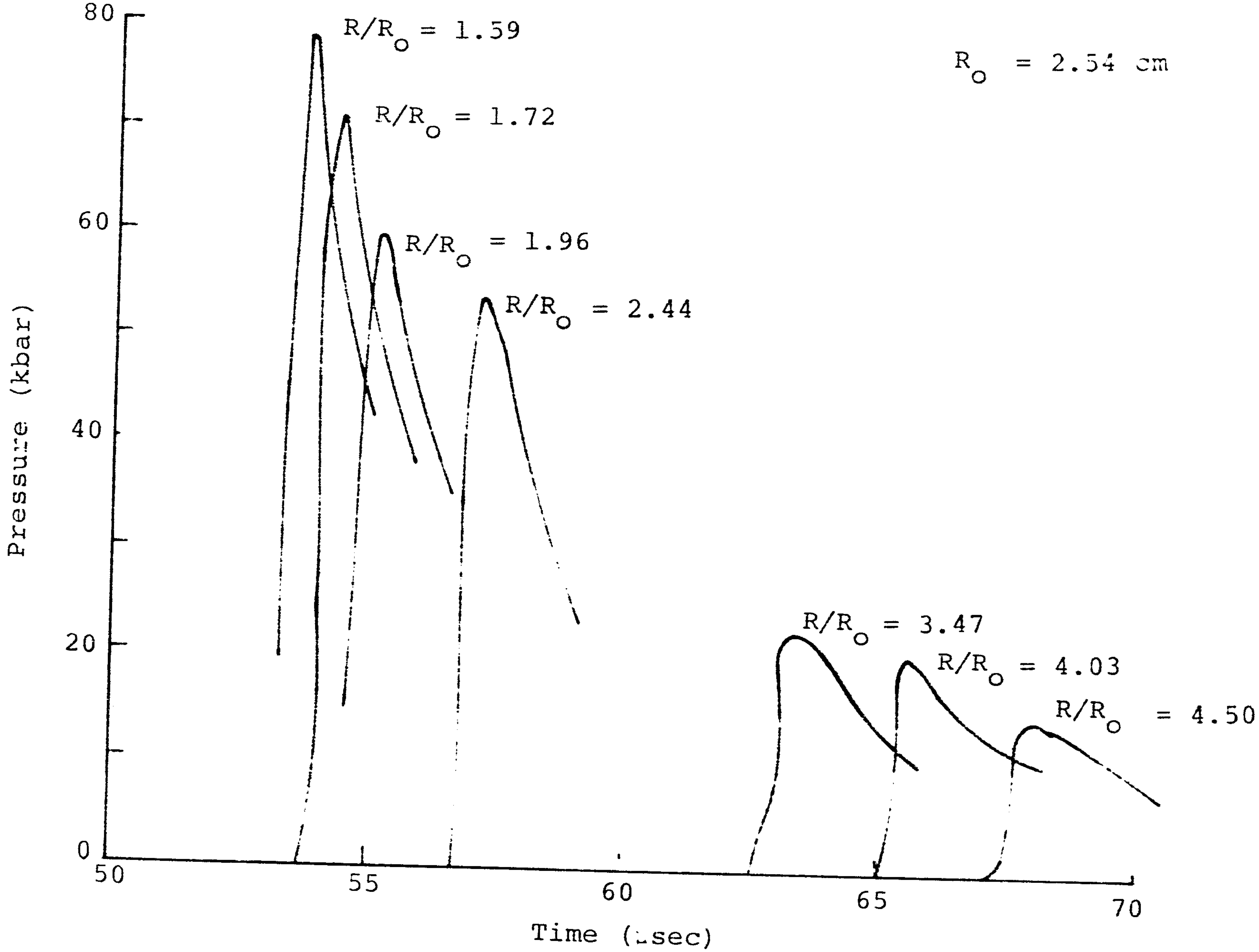

FIGURE 3. OBSERVED STRESS-TIME PROFILES FROM 2.54-cm CAVITY RADIUS SPHERICAL BLOCK TESTS IN BASALT

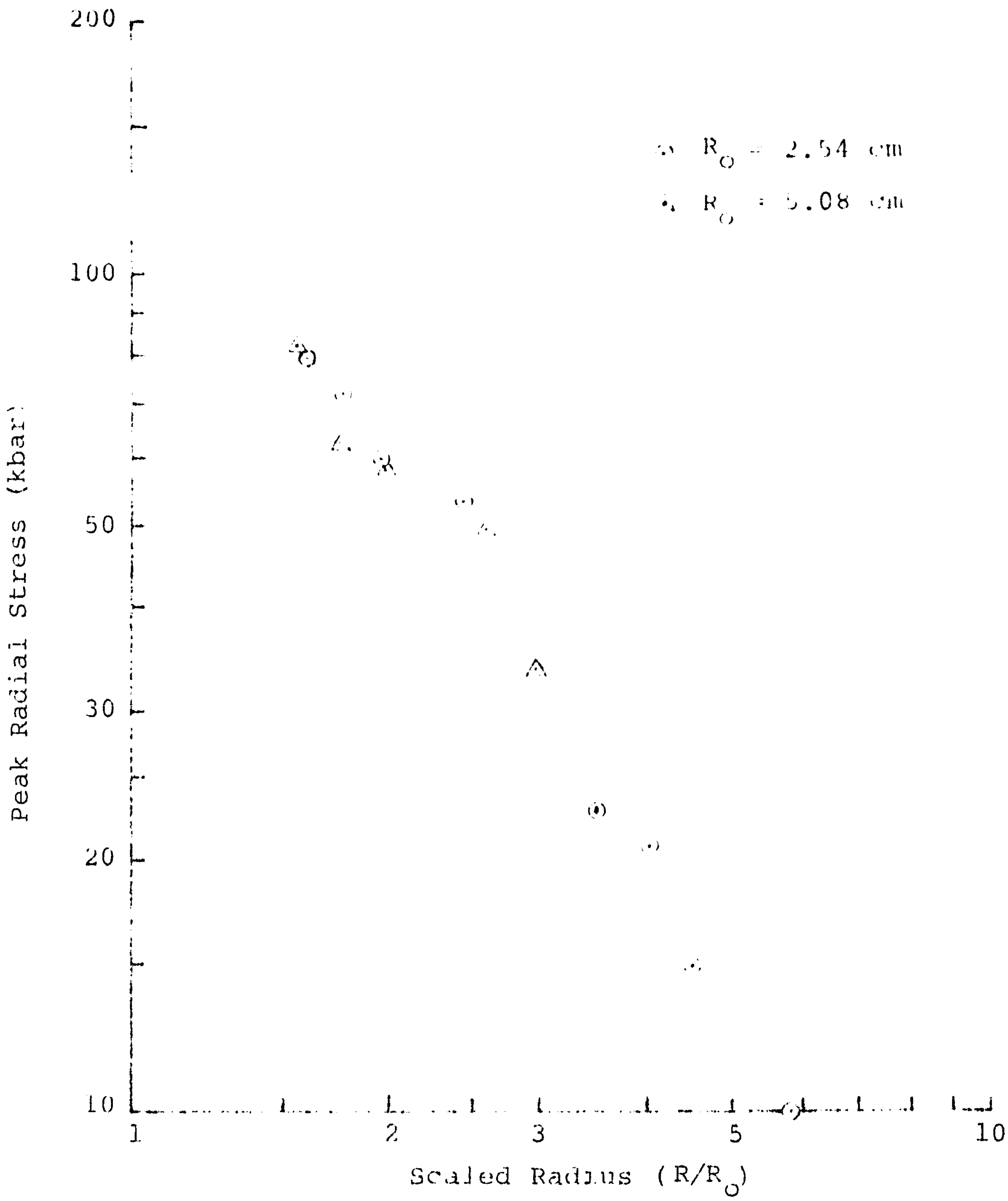

FIGURE 4. OBSERVED PEAK STRESS ATTENUATION

attenuation rate. The attenuation rate is considerably faster than the simple $(R/R_o)^{-1}$ dependence required for elastic spherical divergence and results from irreversible work done on the basalt. The significance of various attenuation rates is discussed in a later section in conjunction with the basalt modeling work.

B. ZERO-PRESSURE STATIC MEASUREMENTS

The densities of the core samples removed from the basalt blocks used in the spherical tests were measured at 2.82 g/cm^3 ± 0.5%. This density is identical to that reported by Gregson for Vacaville basalt. Gregson also reported a porosity of about 3% due to vesicles. Attempts were made to measure the porosity of our basalt samples. The samples were thoroughly dried in a vacuum oven, weighed, and subsequently submerged in boiling water for 24 hours The apparent mass increase recorded for several samples after submersion was less than 0.5%, corresponding to a porosity of about 1.5%. The existence of additional porosity in our samples must then have been due to vesicles that cannot communicate with the outside surface of the rock.

A series of ultrasonic wave speed measurements was performed on a large basalt sample. Using an exploding bridgewire as the source of a strong elastic pulse, a quartz transducer was used to monitor arrival times as a function of distance. The measured P-wave speed was 0.56 cm/μsec. Using a Poisson's ratio of 0.25, the bulk and shear moduli were calculated to be 0.492 and 0.295 Mbar respectively. These values of elastic constants were used in the basalt model analysis.

SECTION IV

ANALYTIC MODEL FOR BASALT

The basic tool used in determining the analytic model is Physics International's one-dimensional, time-dependent elastic-plastic computer code, POD. This code solves, in finite-difference form, the equations of motion in plane, cylindrical, or spherical geometry for an elastic-plastic solid. A large variety of equations of state, including a variety of yield models, are available in the code. We have used this code to correlate calculated wave shape and peak stress attenuation to the observed data presented in Section III by adjusting in an iterative manner, the model used for the equation of state.

The model developed was suggested by the fact that the minerals in basalt, of which plagioclase feldspar is the major constituent, undergo an irreversible phase transition to a higher density form under shock compression (Reference 15). The two-wave structure reported by Gregson can be explained with a phase transition model; further, it defines the upper limit of the low-pressure phase as 0.050 Mbar. For higher stress levels, the dominant influence on the material behavior appears to be the irreversibility of the phase transition. This phenomenon was observed by Rosenberg et al at SRI (Reference 16) in shock wave experiments on fused quartz and tuff. The proposed model for basalt is shown in Figure 5 and includes the pressure-compression data of Gregson and Jones. The pressure-compression curve is divided into three regions representing a low-pressure phase, a mixed phase, and a high-pressure phase. The low-pressure phase, extending from 0 to 0.050 Mbar and determined from the wave speed measurements and Poisson's ratio, is described by the equation

$$P_L = 0.492\,\mu + 0.570\,\mu^2 + 1.50\,\mu^3$$

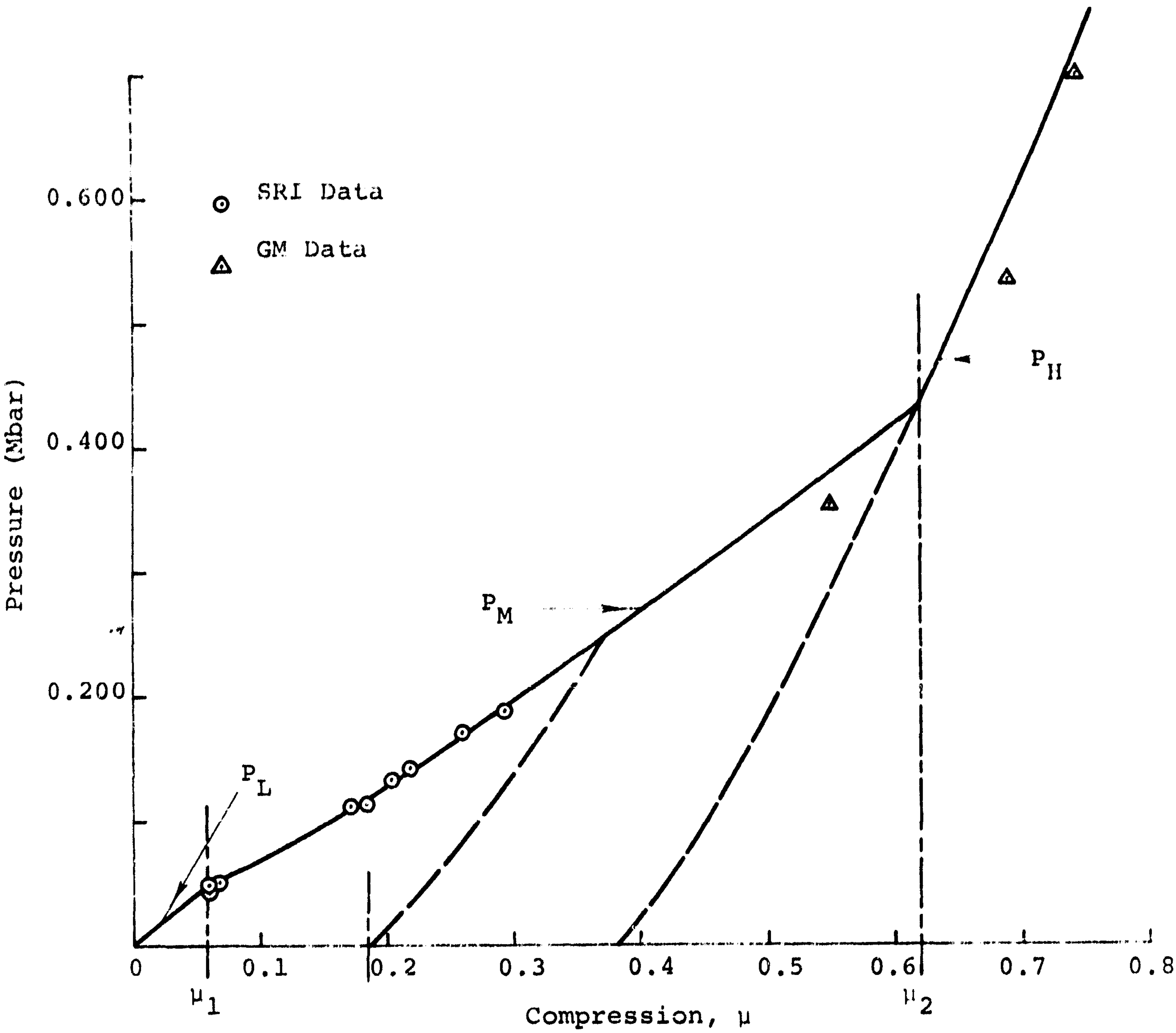

FIGURE 5. IRREVERSIBLE PHASE TRANSITION MODEL FOR BASALT

where $\mu = \rho/\rho_o - 1$. The zero-pressure density of the low-pressure phase, ρ_o, was taken as 2.82 g/cm^3. The mixed-phase region extends from 0.050 to 0.435 Mbar and was fitted to pass through the Hugoniot data of Gregson and join with the high-pressure data of Jones. The equation that describes the mixed-phase region is

$$P_M = 0.020 + 0.50\,\mu + 0.278\,\mu^2$$

For peak pressures greater than 0.435 Mbar, the basalt has completed the transition to the high-pressure phase and is described by the equation fitted to the Hugoniot data of Jones.

$$P_H = 1.98\,\mu_H + 2.97\,\mu_H^2$$

where $\mu_H = \rho/\rho_H - 1$ and ρ_H is the zero-pressure density for the high-pressure phase, 3.90 g/cm^2. This density is determined by the intercept of the (P_H, μ) curve with the μ axis.

The three equations presented above describe the solid curves in Figure 5 and were used to calculate peak stress attenuation. If one assumes a hydrodynamic reversible model (loading and unloading take place along the curves just described and the yield stress is zero), the calculated peak stresses do not attenuate nearly as rapidly as do the observed data (Reference 17). On the other hand, when an irreversible phase transition model was assumed, the calculated stress attenuation rate provided a close fit to the data. Furthermore, the attenuation rate for peak stresses above 0.050 Mbar was essentially independent of the particular yield model, being dominated by the irreversibility of the phase transition. In the mixed-phase region the irreversibility is taken into account by the fact that the material unloads or relaxes along paths that vary in slope, shown as dashed lines in Figure 5. The particular unloading path is a function of the peak pressure attained. For pressures greater than 0.435 Mbar, the material relaxes to zero pressure along the P_H,

μ curve, while for peak pressures less than 0.050 Mbar the material unloads along the P_L, μ curve. For peak pressure levels in the mixed-phase region, 0.250 Mbar for example, the unloading curve is the dashed line intercepting the P_M, μ curve at 0.250 Mbar. The slope of the unloading curve in the mixed phase region is determined point-by-point from the function $dP(\mu)/d\mu$ evaluated as a linear function of μ between $(dP_L/d\mu)_{\mu_1}$ and $(dP_H/d\mu)_{\mu_2}$.

Having established that the yield model is of relatively small importance in determining stress attenuation rates above 0.050 Mbar (Reference 17), a hydrodynamic yield model was assumed for the mixed- and high-pressure phases and effort was concentrated on the low-pressure phase. An additional justification for assuming a hydrodynamic yield model in the mixed- and high-pressure phases is that the mineral compaction associated with phase transition suggests a loss of cohesion between adjacent material elements.

Figure 6 presents calculated and observed stress attenuation data, showing the effect of various yield models in the low-pressure phase. The hydrodynamic yield model (Y = 0) does not provide a sufficiently high rate of peak stress attenuation. On the other hand, a Coulomb-Mohr yield model, Y = 1.4 + 1.38 P (kbar) as obtained from triaxial strength data (References 18, 19, 20), results in too rapid stress attenuation. The best fit to the attenuation data was obtained by using a Von Mises yield of Y = 1.0 kbar.

The stress-time profiles calculated using the irreversible phase transition model with a 1.0-kbar Von Mises yield model in the low-pressure phase are compared with experimental profiles in Figure 7. The area under the stress-time curve represents the impulse delivered to the material by the shock wave and thereby determines the resulting material displacement, i.e., crater size. We feel that the computed stress profiles are in good agreement with the observed profiles and

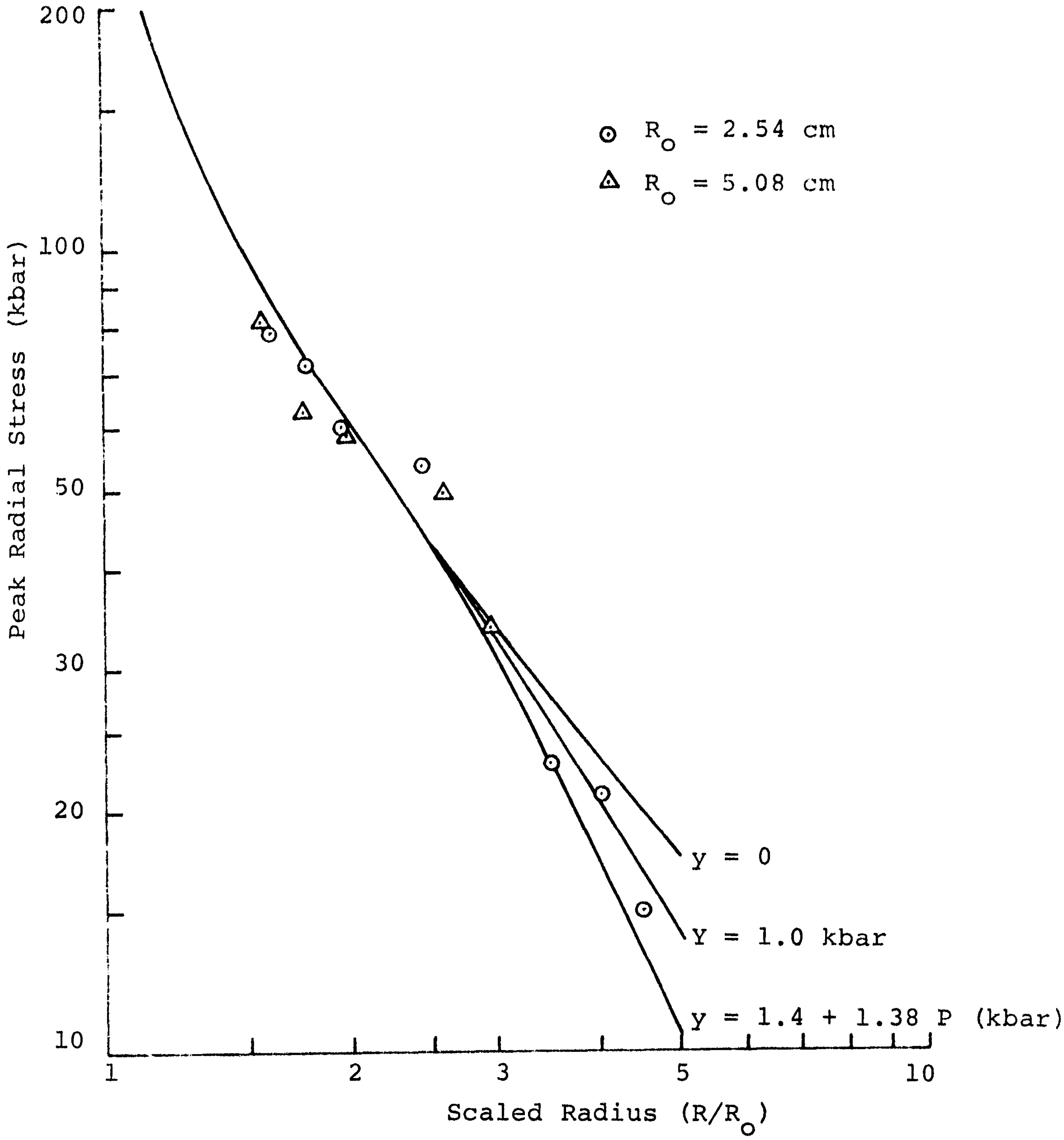

FIGURE 6. CALCULATED AND OBSERVED PEAK STRESS ATTENUATION

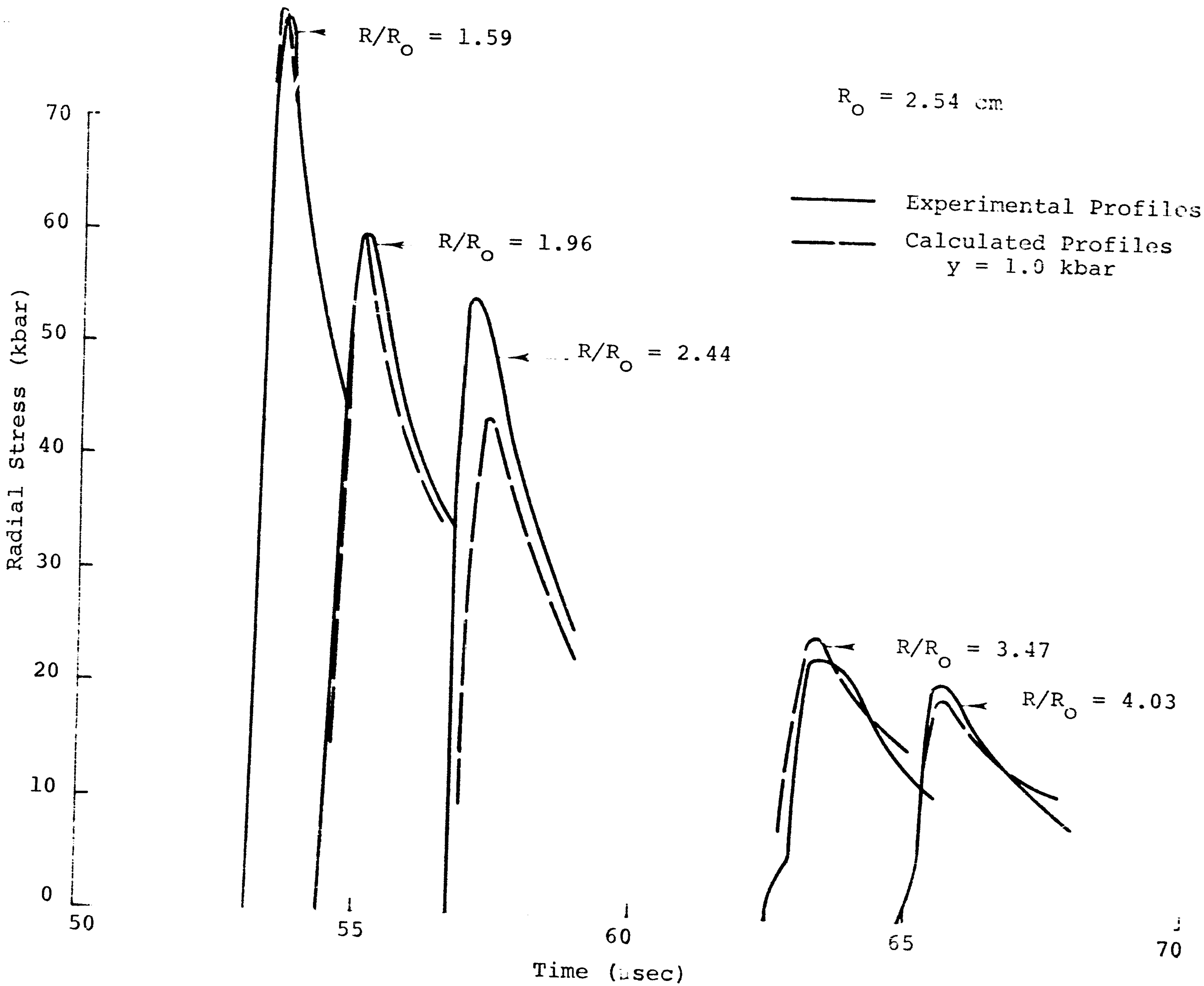

FIGURE 7. COMPARISON OF EXPERIMENTAL AND THEORETICAL STRESS PROFILES

that the basalt model presented here, although not unique, provides a reasonable material description for computing divergent shock waves in basalt.

SECTION V

DESCRIPTION OF HYPERVELOCITY IMPACT EXPERIMENTS

A. IDEAL OPERATION OF EXPLOSIVE DRIVER

The linear explosive driver represents a technique whereby a substantial portion of the chemical energy of an explosive is converted in a controlled manner to the kinetic and internal energy of a gas. Basically, the energy densities in the gas are produced by a strong shock generated by the progressive collapse of a tube. The collapse of the tube is such that it may be represented as a piston propagating into a gas. The ideal model used to describe implosive driver operations is quite similar to that used to explain the basic discontinuous motion produced by a shock wave.

The operational characteristics of the linear explosive driver are shown in Figure 8. A thin-walled metal tube, the pressure tube, containing the driver gas is surrounded by a chemical explosive. After the explosive is initiated, a detonation wave propagates in the explosive along the outside of the metal tube. The pressure behind the detonation wave accelerates the wall of the tube in toward the axis, sealing the tube and forming a conical-shaped piston (Figure 8b). The velocity of the piston D equals the detonation velocity of the explosive. The motion of this piston generates a strong shock wave in the stationary column of driver gas. If the gas behaves ideally and has a constant ratio of specific heats γ, then the velocity of the shock wave S is $(\gamma+1)D/2$. The position-time histories of the piston and shock wave are shown in Figure 8c for an ideal driver gas ($\gamma = 5/3$). These trajectories are presented in the dimensionless coordinates

$$\bar{x} = \frac{x}{d} \quad \text{and} \quad \bar{t} = \frac{Dt}{d}$$

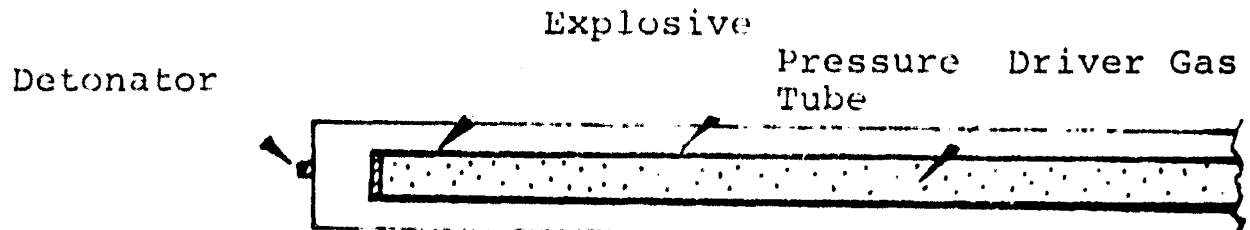

a. Time = 0, Before Initiation of the Explosive

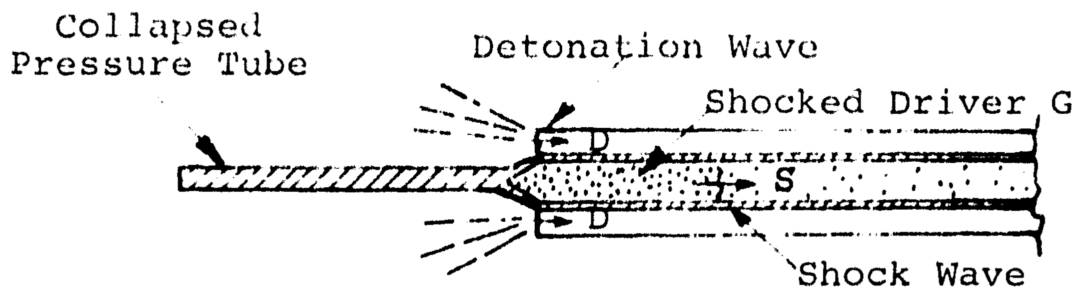

b. Time = $\bar{t}_1$, After Initiation of the Explosive

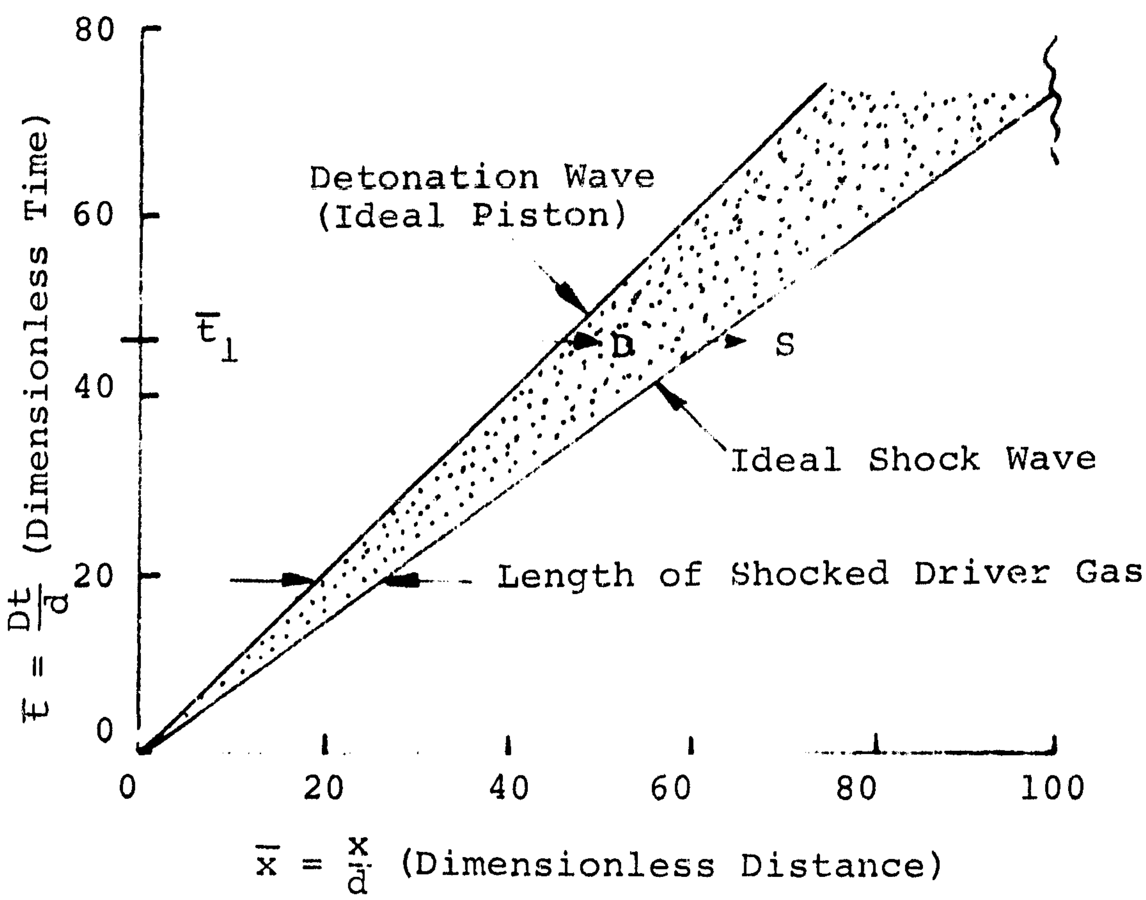

c. Position-Time History of Shock and Detonation Wave

FIGURE 8. IDEAL OPERATION OF THE LINEAR EXPLOSIVE DRIVER

Here x and t are the distance and time after the shock wave begins to move ahead of the detonation wave, d is the internal diameter of the pressure tube, and D is the detonation velocity of the explosive. These coordinates facilitate the comparison of systems having different dimensions or different detonation velocities.

The pressure P_2 in an ideal gas behind a strong shock wave is given by the conservation equations as

$$P_2 = P_1 + \rho_1 \left(\frac{\gamma + 1}{2}\right) D^2$$

where P_1 and ρ_1 are the pressure and density of the stationary gas ahead of the shock. This relationship indicates how conditions in the shocked gas can be varied over a considerable range of gases (γ), initial loading densities (ρ_1), and explosive (D).

When an explosive driver is used to launch projectiles the shock wave in the driver gas is reflected from an area change or breech (in a chambered gun). The reflected shock brings the gas essentially to rest, converting its available kinetic energy to additional internal energy. This process produces a reservoir of gas having an extremely high energy density and sound speed. This reservoir of gas is then used to accelerate the projectile.

The operation of a chambered explosively driven gas gun, as used in this program, is illustrated schematically in Figure 9. The pressure tube is initially filled with 60 atm of helium, while the barrel contains 1 atm of helium. The projectile is positioned three body diameters downstream of the breech. As the high pressure behind the detonation wave collapses the pressure tube, a 6-kbar shock is driven into the stationary helium gas as depicted in Figure 9b. On reflection from the breech, the shock forms a reservoir of high-pressure (≈ 36 kbar)

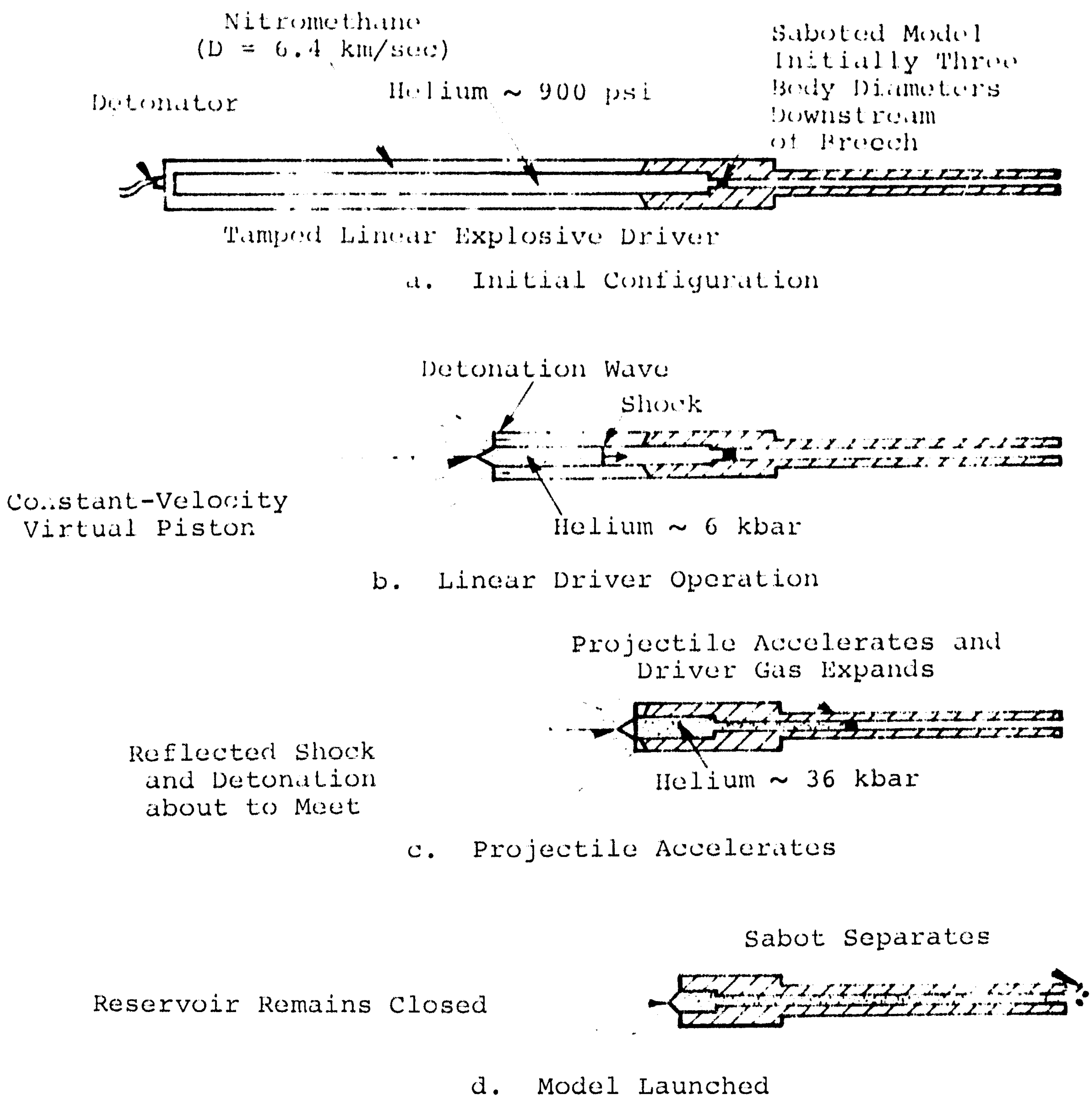

FIGURE 9. OPERATION OF A SIMPLE EXPLOSIVELY DRIVEN LAUNCHER

gas which accelerates the projectil A slight base pressure on the projectile as it leaves the barrel causes the sabot pieces to separate from the enclosed model, as illustrated in Figure 9d. A more complete discussion of the operational details of explosively driven launchers can be found in References 6 through 8.

The 6.4-km/sec launcers used in this program have a 100-cm-long barrel with a nominal 1.71-cm bore. The overall length of the launchers is 209 cm and each requires 5.5 lb of nitromethane.

B. PROJECTILE-SABOT DESIGN

Projectile behavior is strongly coupled to the gas dynamic cycle of the launcher and the dynamic response of the barrel. Computer techniques (Reference 21) are capable of accurately predicting dynamic projectile-launcher interaction, thus avoiding trial-and-error design methods. Because an existing launcher design was used in this program, the gross projectile behavior had been previously integrated with the launch cycle; however, the details of the sphere and sabot geometry were chosen to minimize residual distortion of 1.0-g sphere.

The two sabot pieces and the sphere were made of a lithium-magnesium alloy (LA141A), which has been used extensively at Physics International as a projectile material. Its low density (1.38 g/cm^3) and relatively high yield strength (13,000-15,000 psi) lead to high velocity as well as good resistance to fragmentation and distortion. During the launch cycle, however, the projectile is subjected to base pressures of roughly 36 kbar, many times the projectile yield strength. Under these conditions of high axial compression the projectile behaves plastically and its lateral surface is forced against the walls of the launcher barrel. As the surface of the sabot erodes due to wall friction, the high base pressure continually forces more material against the barrel wall. The mass loss to erosion is accounted for by a decrease in the overall length of the projectile. The net deformation within the sabot package is the result of the radially outward material flow and accompanying length contraction. The deformation is greater toward the base (rear) of the projectile because the time-integrated stresses are larger there than at the front of the projectile. For this reason, the sabot was designed with the sphere positioned toward the front of the sabot. A longitudinal cross section of the assembled sabot is shown in Figure 10. The mass of the sphere was 1.0 g and the total mass of the sphere and sabot pieces was 4.2 g.

C. DIAGNOSTIC RANGE

A nonexpendable shot stand was constructed that provided precise positioning of the launcher and target. The launcher barrel was clamped to two adjustable supports, providing a fine adjustment for bore-sighting the gun with the desired point of impact on the target. The 195-cm distance between the launcher muzzle and the target face comprised an atmospheric free-flight diagnostic range. A stripper plate, designed to stop the sabot pieces without perturbing the sphere, was positioned approximately 165 cm down range from the launcher muzzle. The sphere passed through a 3.8-cm-diam hole in the stripper plate while the sabot pieces, separated from the sphere, impacted against the stripper plate. Range diagnostics used to monitor position-time points of the projectile included doubly aluminized Mylar shorting switches, a high-speed streaking camera, and three pulsed X-ray units. The resulting radiographs, in addition to giving position-time data, presented visual information as to the separation of the sabot pieces, condition of the sphere, and in some instances ejecta thrown off the target during the cratering process.

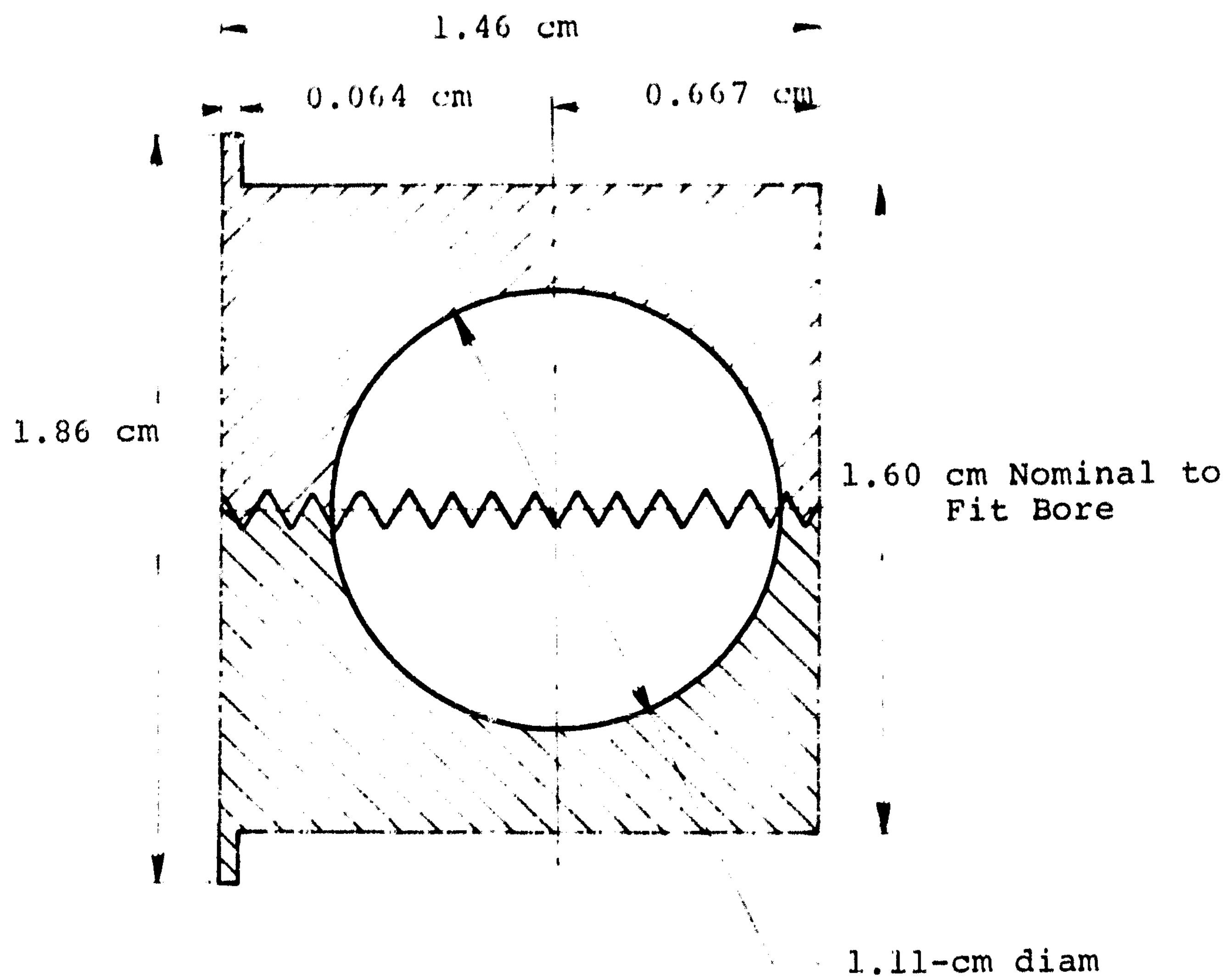

FIGURE 10. LONGITUDINAL SECTION OF SABOT PACKAGE

D. BASALT TARGET INSTRUMENTATION

1. Embedded Manganin Gauges

The impact targets were fabricated from basalt rock samples. Piezoresistive manganin gauges were embedded in targets at various depths from the front face by sandwiching the gauge between two slabs of basalt. The manganin gauge configuration was similar to that shown in Figure 2, with the notable exception that a copper-nickel gauge was not employed. Typically, two independent manganin gauges were incorporated into each target. One gauge was positioned directly behind the point of impact and one off-axis but along the same plane. This configuration allowed stress profiles at two different distances from the point of impact to be obtained from each shot.

A manganin gauge record obtained on an impact test is shown in Figure 11. The upper trace is monitoring the output voltage from an on-axis manganin gauge 2.97 cm behind the point of impact. The vertical sensitivity is 2.0 V/cm and the horizontal sweep speed is 1.0 μsec/cm. The first rise of roughly 1.3 cm represents the power supply turn-on. The second rise, occurring 4 cm from the start of the trace, is due to the stress pulse emanating from the projectile impact point. The final sharp fall-off toward the end of the trace indicates gauge failure. The lower trace is simultaneously displaying the same gauge signal at an increased vertical sensitivity of 0.5 V/cm. The baseline is suppressed so that the power supply turn-on brings the trace on scale. The piezoresistive calibration factor allows the voltage-time profile to be translated into a stress-time profile. For the sample trace in Figure 11, the peak stress as calculated in this manner was 50.8 kbar.

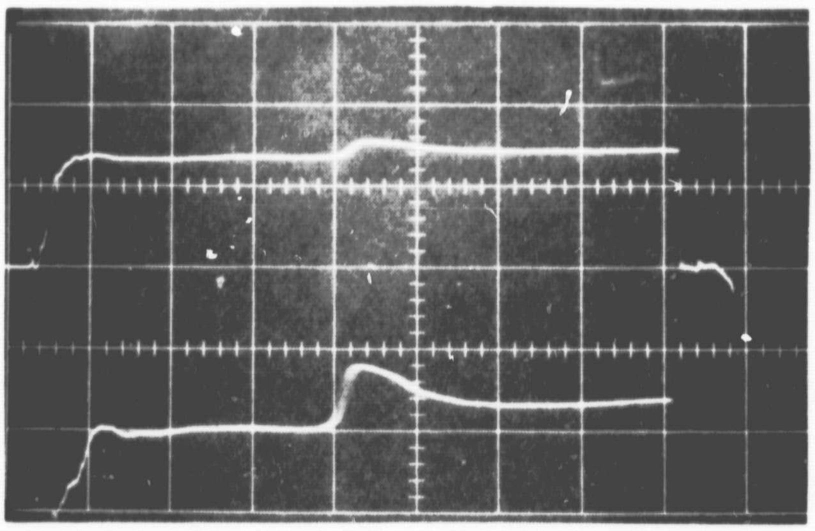

Vertical Sensitivity
2.0 V/cm

Vertical Sensitivity
0.5 V/cm

Horizontal Sweep
Speed = 1.0 cm/μsec

FIGURE 11. TYPICAL MANGANIN GAUGE RECORD

2. Crater Observation

Because embedded gauges require the target to be composed of two slabs of material held together by epoxy, it is not possible to obtain stress profiles and meaningful final crater data from the same target. Therefore, two targets were designed and constructed from a large block of basalt to obtain a final crater. A slab of solid basalt 35.5 by 35.5 by 10.0 cm was surrounded on five sides with 1.27-cm-thick aluminum plates, leaving a 35.5- by 35.5-cm face of basalt exposed. The aluminum plates provided a shock impedance match with the basalt, reducing the probability of spalling the sides of the basalt block. Vacuum grease was applied between the basalt and aluminum to eliminate any voids due to surface irregularities. The aluminum plates were squeezed against the basalt while concrete was poured around the plate assembly, leaving only the basalt face exposed. The concrete block containing the basalt target measured 66.0 by 66.0 by 30.5 cm and provided inertial containment for the aluminum plates and basalt. An assembly of this design was used for a 6.4-km/sec and a 11.6-km/sec impact.

SECTION VI

RESULTS OF IMPACT EXPERIMENTS

A. LAUNCHER PERFORMANCE

A total of nine hypervelocity impact tests (Shot Nos. 397-10 to 395-18) were conducted during this program. The first shot, (Shot 395-10) launched a saboted 1.5-g magnesium-lithium alloy sphere to verify the launcher and projectile design. At this point in time the 1-g spheres were not available; thus the larger spheres were used. Because the sabot pieces must be thinner to accommodate a larger sphere, the use of a 1.5-g sphere represents a more severe test of projectile integrity than the 1-g sphere.

The result of the shot was that the sphere while launched to an abnormally high velocity of 8.1 km/sec, was damaged during the gun cycle. The attained speed considerably exceeded the anticipated speed of 6.4 km/sec. Although the driver diagnostics indicated a normal detonation and shock trajectory, a driver malfunction was speculated to have occurred after the last diagnostic pin reported. A premature detonation of the sensitized nitromethane initiated by exposure to the 6-kbar helium shock would drive a very strong shock into the projectile. This shock would account for both the high speed and broken condition of the projectile. Whereas the nitromethane for this shot was sensitized with 3% ethylenediamine, it was decided that future shots would use nonsensitized nitromethane. An additional result of the initial shot was that the non-expendable shot stand proved a practical concept.

Two small modifications made in the design of the next shot, (Shot 395-11) were: the initial projectile position was moved from two to three body diameters downstream from the area change to provide a more uniform shock loading, and the nitromethane was nonsensitized. A radiograph of the projectile in flight indicated that the 1.5-g sphere was in good condition. The muzzle velocity of the sphere was 6.7 km/sec.

The purpose of the third shot (395-12), was to determine the separation rate of the sabot pieces from a 1-g sphere. This information was necessary for determining the size and position of the sabot stripper plate. By extrapolating the observed sabot separation rate as taken from three in-flight radiographs, it was determined that a free flight of 165 cm from the muzzle of the launcher was required before attempting to strip the sabot pieces. Having successfully launched a 1-g sphere and determined the sabot stripper position and configuration, a series of five identical launchers was fabricated and fired (Shots 395-13 through 395-17) into basalt targets.

A typical position-time plot showing the explosive driver operation and the projectile trajectory is presented in Figure 12. Four pulsed X-ray units are indicated; however, only three of the four positions were used on any one shot. A series of three radiographs of the projectile taken both before and after sabot stripping is shown in Figure 13.

The first radiograph (Figure 13a) shows the sabot pieces separated from and trailing the sphere. In this picture, the sphere was traveling from left to right at 6.5 km/sec, 115 cm (an estimated 175 μsec) downrange from the muzzle of the launcher. Aerodynamic counterpressure is beginning to deform the sabot pieces. The flattened trailing edge of the sphere was characteristic of all projectiles launched during this program and results from the high base pressures experienced during the launch cycle, as previously discussed in Section V-B. Since the deformation of the sphere involves a change in trailing edge geometry, not in energy or momentum, there is a negligible effect on the cratering process.

Figure 13b was taken 145 cm downrange from the launcher and shows the sphere and sabot pieces continuing to separate. In Figure 13c, the sphere is 173 cm from the launcher and has just passed through a 3.8 cm-diam hole in the center of the sabot stripper plate, visible

7037

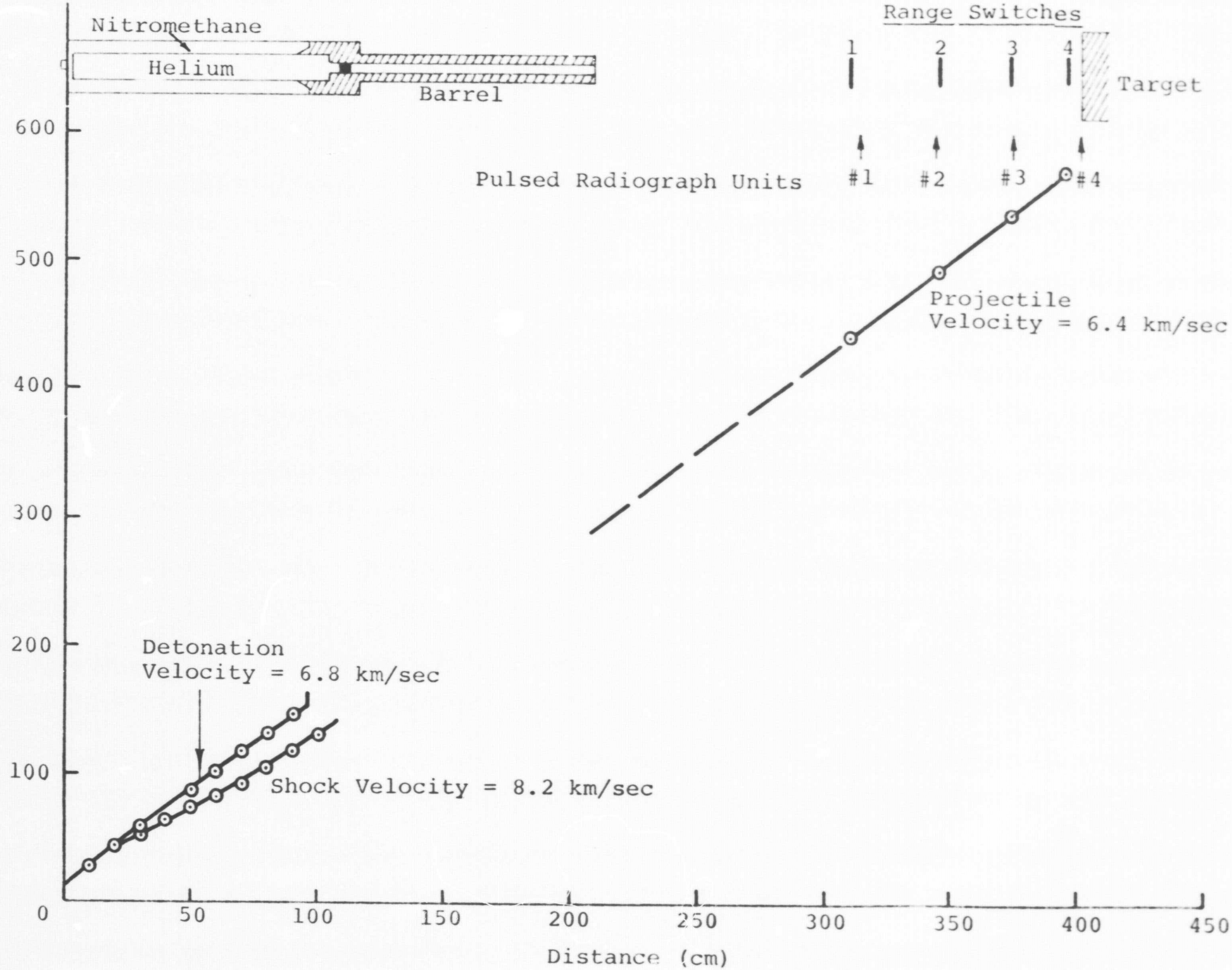

FIGURE 12. TYPICAL POSITION-TIME PLOT FOR 6.4 km/sec LAUNCHER IMPACT TEST

a. Before Stripping,
Sphere 115 cm Downrange

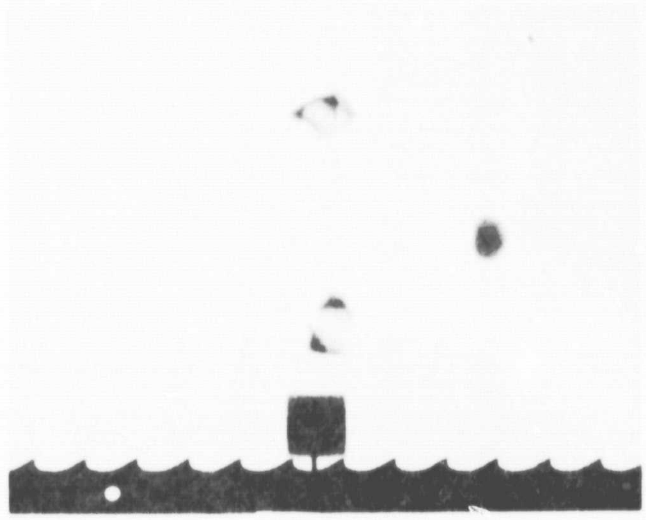

b. Before Stripping,
Sphere 145 cm Downrange

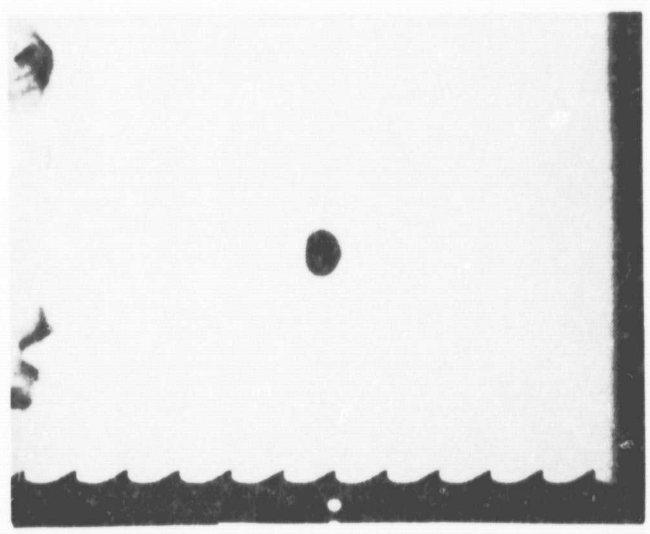

c. After Stripping,
Sphere 173 cm Downrange

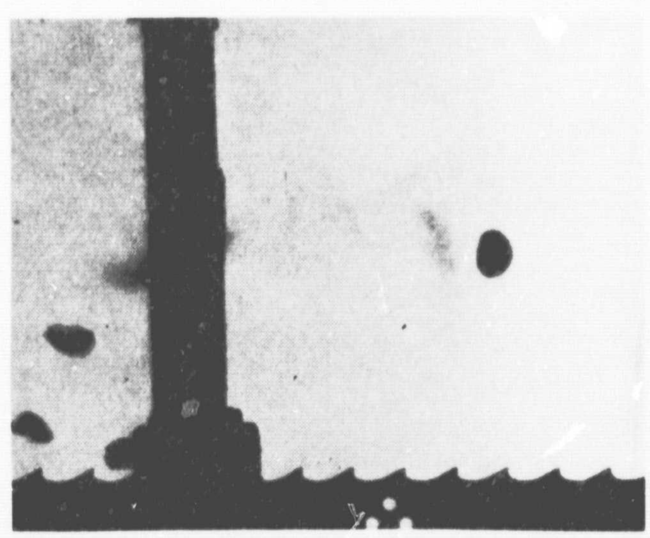

FIGURE 13. RANGE RADIOGRAPHS OF SPHERE BEFORE AND AFTER SABOT STRIPPING

6689

in the center of the radiograph. The sabot pieces, severely broken and having a separation of almost 7.5 cm, are about to impact against the stripper plate. The face of the basalt target was positioned 195 cm from the launcher.

The average impact velocity for Shots 395-13 through 395-17 was 6.4 km/sec. With the exception of Shots 395-14 and 15, the velocity deviations were within 1%. Cratering data from the former shot, however, are of limited value because the sphere grazed the edge of the stripper plate. Although the sphere was shattered, the fragments did not disperse appreciably and stress profiles from the target impact were obtained. However, because the sphere was not following the intended line of flight, the relative position of the point of impact and manganin gauges is not known. Radiographs from the other shots in this series, taken roughly 20 cm in front of the target, indicated that the sphere was in good condition and headed for the intended point of impact.

Having completed the impact tests at 6.4 km/sec, we attempted to impact a basalt target at 12 km/sec. The launcher used for this shot, 395-18, was designed under a concurrent fast-gun development program. It was similar in concept to the 6.4 km/sec launcher, but additional performance was obtained by explosively collapsing the walls of the reservoir section of the driver. This collapse forces more of the high-pressure driver gas behind the reflected shock to expand down the barrel, imparting additional energy to the projectile. Because of the recent design of the launcher, no attempts had been made at firing sabot models. The projectile used in this impact test was a 2-g, right-circular cylinder (magnesium-lithium LA141A) with a length-to-diameter ratio of 1/2. The target, intended to preserve the resulting crater, was a 35.5- by 35.5- by 10.0-cm basalt slab held in an aluminum and concrete assembly as described in Section V-D-2. The target was not instrumented with manganin gauges.

The measured impact velocity for this test was 11.6 km/sec, and the projectile mass at impact was assumed to be 1.6 g, having lost typically 20% to erosion in the launch process. The radiographs of the projectile were lost because of a misfire in a delay circuit. Examination of a streaking camera record revealed two small fragments leading the major portion of the projectile; however, the fragments were overtaken by the projectile before they impacted against the target, which was found broken into several pieces. It is not clear whether the target was broken by the projectile or by the late time impact of a large steel blast shield. Assembly of the basalt pieces showed that a large crater of the anticipated size had been formed.

B. STRESS PROFILES IN BASALT TARGET

Figure 14 shows the relative positions of the intended point of impact and manganin gauges. The depth between the point of impact and on-axis gauge positions varied from 0.52 to 4.98 cm. The off-axis gauges were placed at the same depths from the front face, but along a line drawn from the point of impact at a 45-deg angle with the target face. Therefore the distance from point of impact to off-axis gauges varied from 0.74 to 7.05 cm. The measured peak stresses ranged from 263 to 11 kbar. Since the on-axis gauge is located a minimum distance from the intended point of impact, all errors in stress level due to misalignment of the impacting sphere and target resulted in a reduction of the observed stress level. The maximum angular variation of the projectile was observed to be 0.7 deg. In some instances the peak stress observed at the on-axis gauge was lower than that at the off-axis gauge, implying that the point of impact was closer to the off-axis gauge. It was not envisioned in the design stage of the program that 0.7-deg angular deviations of the projectile would be encountered. This inaccuracy of the projectile trajectory is likely related to the sabot separation process. In future shots a redesigned sabot would be used, perhaps consisting of four pieces of precisely the same mass.

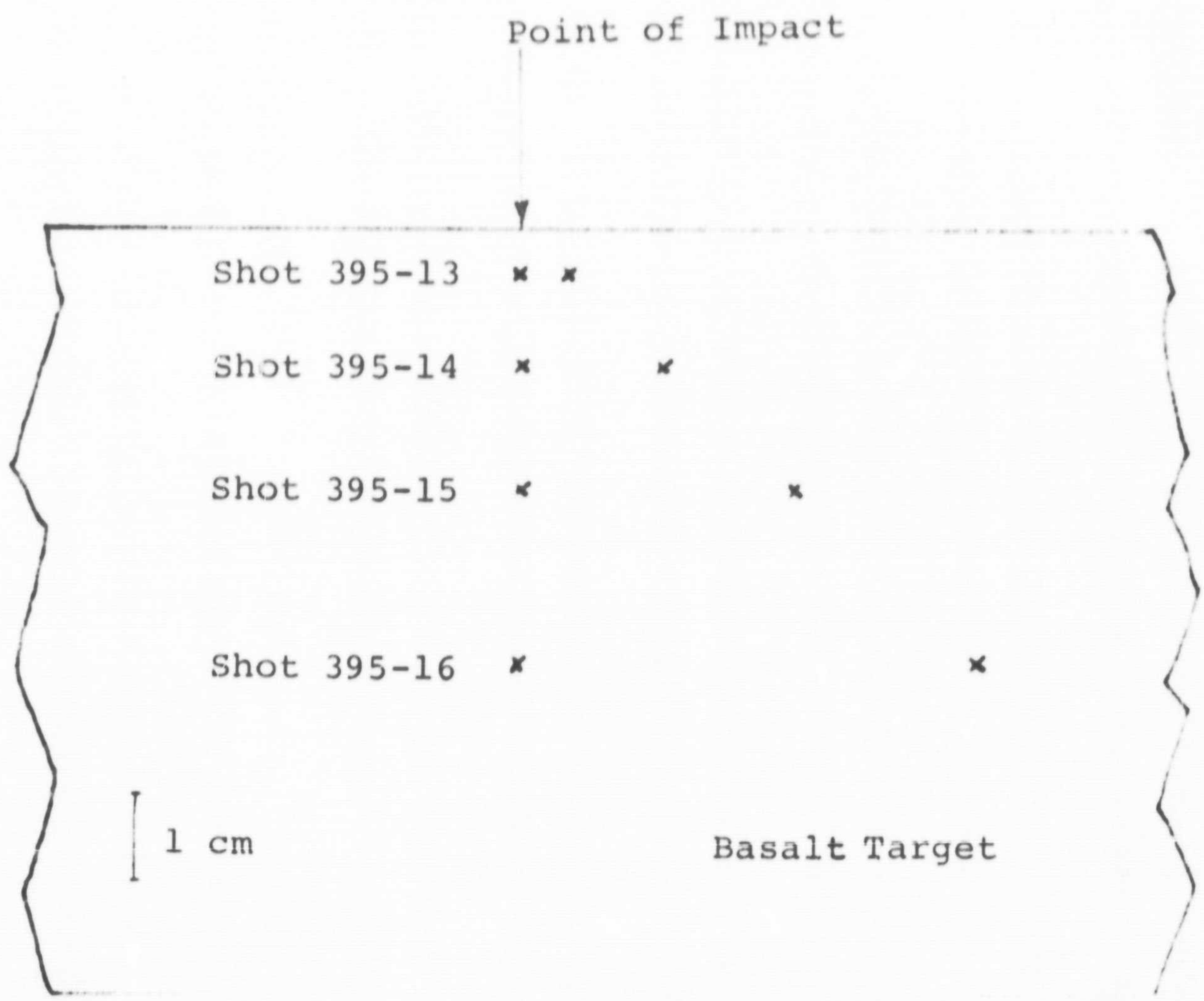

FIGURE 14. RELATIVE LOCATIONS OF EMBEDDED MANGANIN GAUGES IN BASALT TARGETS

All of the peak stress data are plotted in Figure 15 as a function of scaled radius, where r_o was taken as the radius of the impacting sphere (r_o = 0.556 cm). An estimated linear best fit has been drawn through the data points. Because the precise point of impact cannot be determined (which can introduce large errors in the scaled radius), the two abnormally low data points at scaled radii of 2.82 and 7.55 were ignored when estimating the best fit. The flat plate impact stress, calculated from the estimated Hugoniots for basalt and magnesium-lithium LA141A, is 500 kbar. The linear fit to the attenuation data in Figure 15 intercepts the 500-kbar level at a scaled radius of 1. At the same radius the experimental data indicate a stress of roughly half this magnitude. It is interesting to compare this result with a two-dimensional, time-dependent code calculation performed at Physics International (Reference 22) of the impact of an aluminum sphere moving at 7.32 km/sec, against a semi-infinite aluminum target. The initial configuration for the calculation is shown in Figure 16. The calculated stress attenuation rate is shown by the solid line in Figure 17, along with experimental data obtained by General Motors (Reference 23) for the identical aluminum impact cratering experiment. The dashed extension of the calculation for scaled radii less than 1.0 is an estimate based on the magnitude and duration of the flat plate impact stress. The calculated stress level at a radius of 1 is roughly half the flat plate impact value, a situation similar to that observed in our basalt experiments. Also, the linear fit to the data extrapolates to the flat plate impact stress level at a scaled radius of 1. The falling off of the calculated attenuation at large radii is due to the zoning of the problem.

The best fit to the attenuation data shows that the peak stress decays as $(r/r_o)^{-1.42}$. This attenuation rate is comparable with that determined in the basalt modeling experiments described in Section III-A. The crater depth, as measured in Shot 397-17, is plotted in Figure 15 in terms of scaled radius. At this on-axis depth, the peak stress has

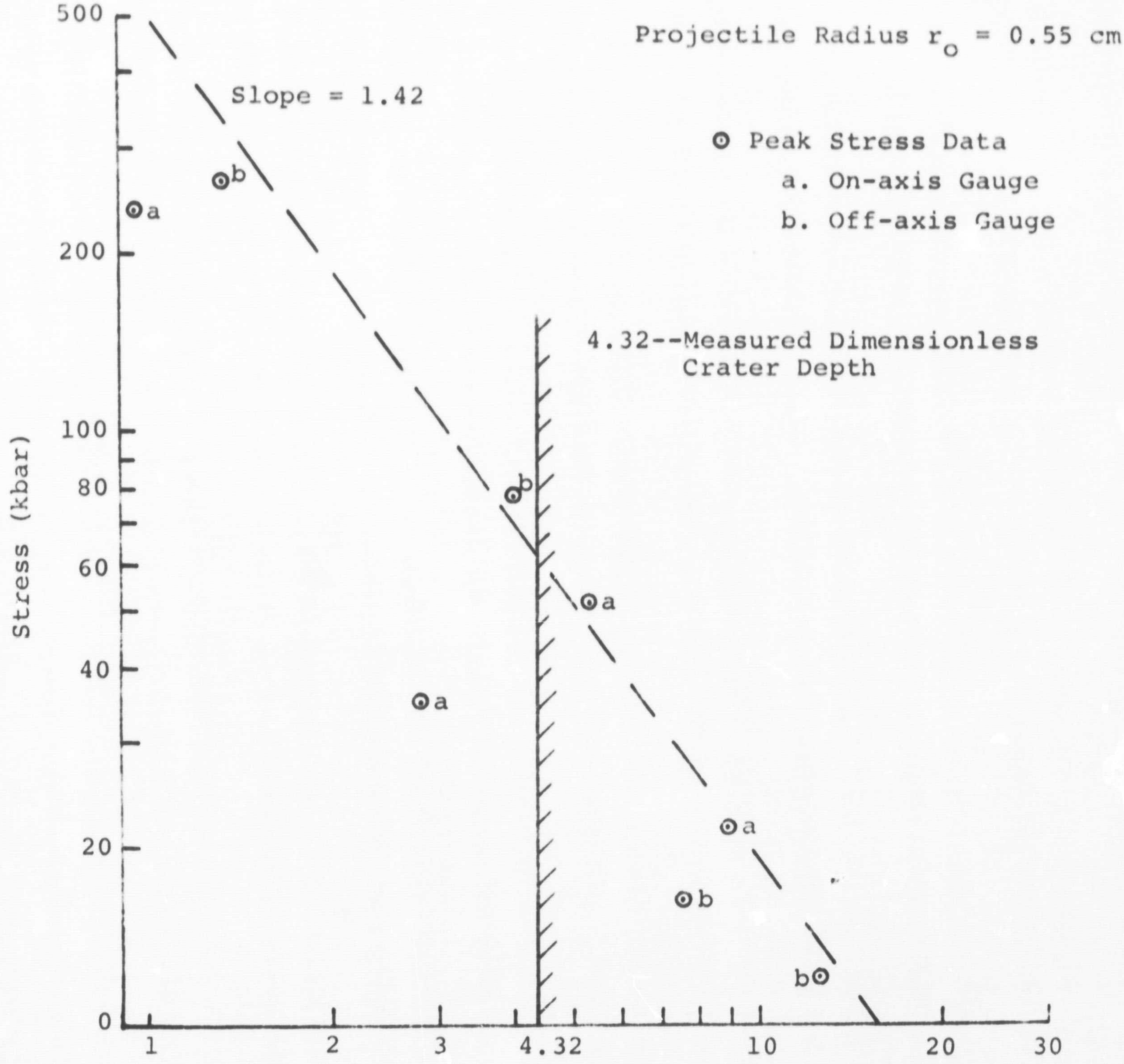

FIGURE 15. STRESS ATTENUATION IN BASALT TARGETS AS A FUNCTION OF SCALED RADIUS

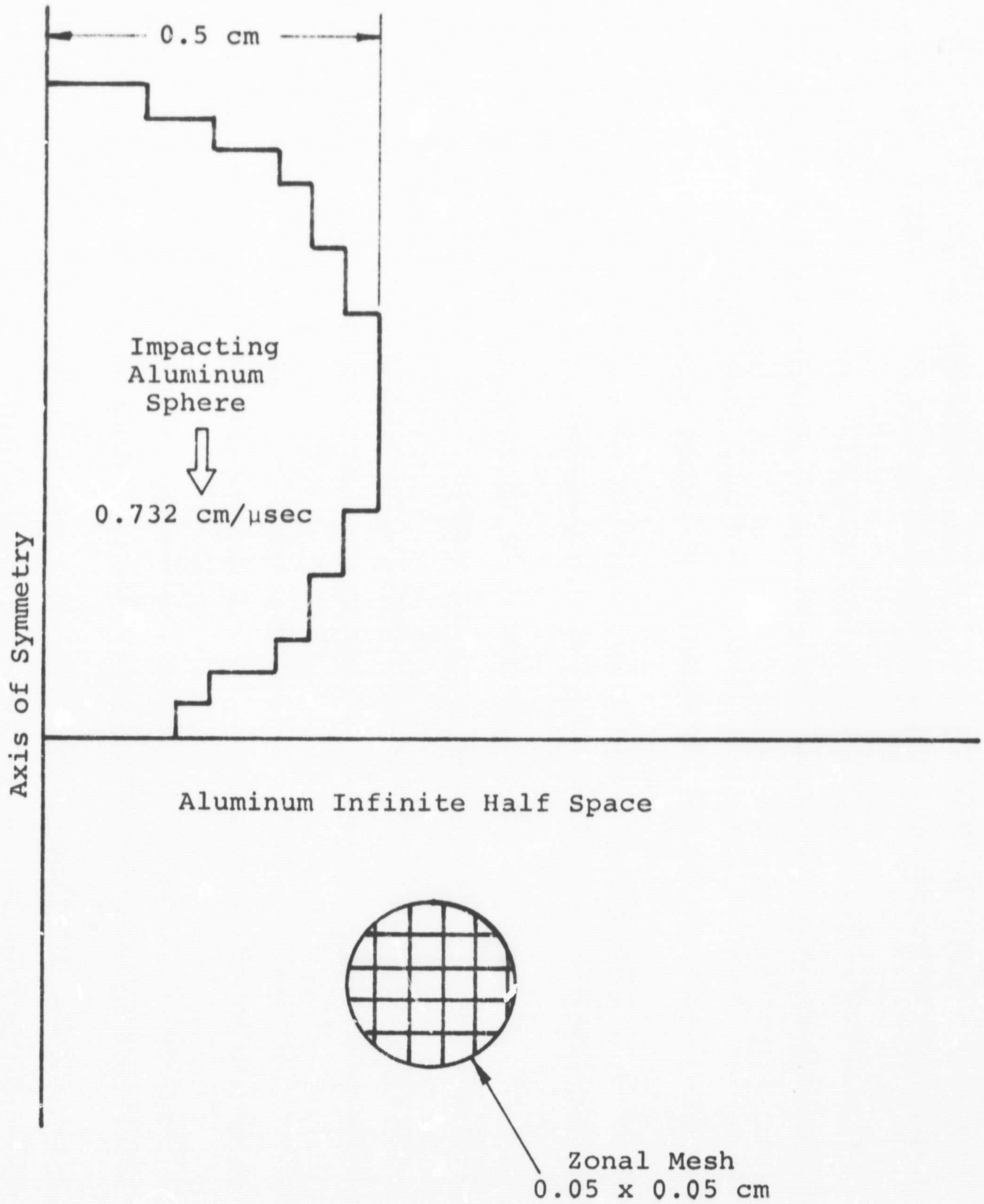

FIGURE 16. ORIGINAL CONFIGURATION FOR IMPACT CALCULATION

2658

7086

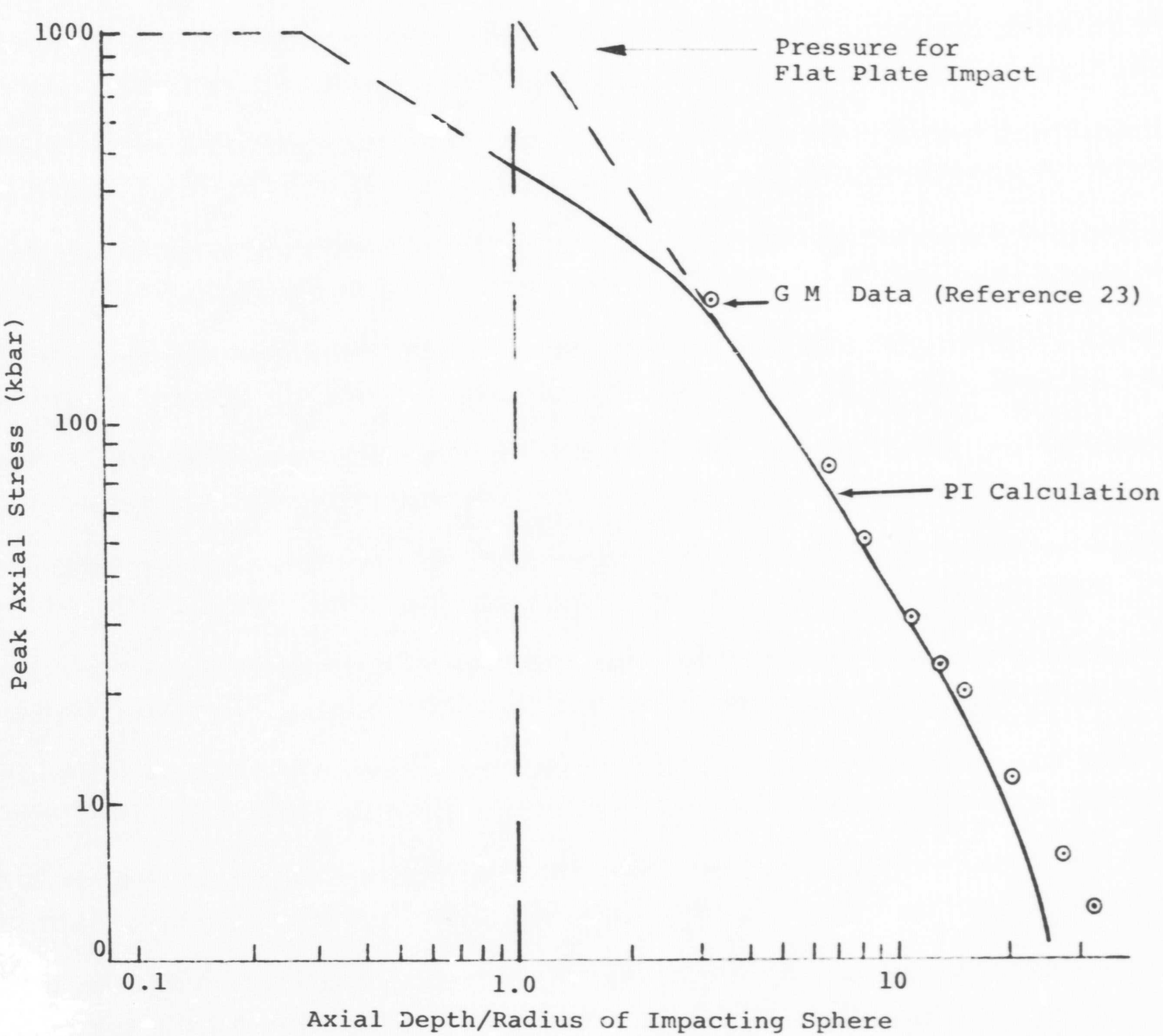

FIGURE 17. CALCULATION OF 1-cm-diam ALUMINUM SPHERE IMPACTING 1100-0 ALUMINUM TARGET AT 7.32 km/sec

attenuated to roughly 60 kbar. This stress level is approximately that at which the phase transition in basalt begins. An admittedly simple explanation of this correlation follows: As various mineral constituents of basalt undergo a phase transition to a more dense form, the basalt loses its competence and is ejected from the target. However, as the peak stress (or more likely some time-integrated stress) attenuates below the minimum level necessary for phase transition, the basalt will remain competent, with any further increase in crater depth being correspondingly small.

The impact study at General Motors (Reference 23) of peak stress attenuation observed in 1100-0 aluminum targets showed that the final crater depth in aluminum occurred at a peak stress level of roughly 70 kbar. Since the shock impedance of aluminum is very close to that of the low-pressure phase of basalt, the material displacement in a uniaxial strain configuration is expected to be similar for the two materials. Therefore one would expect the material flow along the axis of impact to stagnate at roughly the same stress levels in basalt and aluminum. By comparison then, it is plausible that a negligible increase in the basalt crater depth will occur after the peak stress has attenuated into the low-pressure phase.

C. BASALT CRATER OBSERVATION

On two of the shots in the 6.4-km/sec series, a pulsed radiograph unit was used to observe ejecta thrown from the face of the basalt target. Figure 18 is a radiograph of the target in Shot 395-16 taken 7.3 μsec after projectile impact. A dimensional reference is provided by the 1.27-cm spacing of the saw teeth. This target was instrumented with manganin gauges; a lead can be seen protruding from the top of the block.

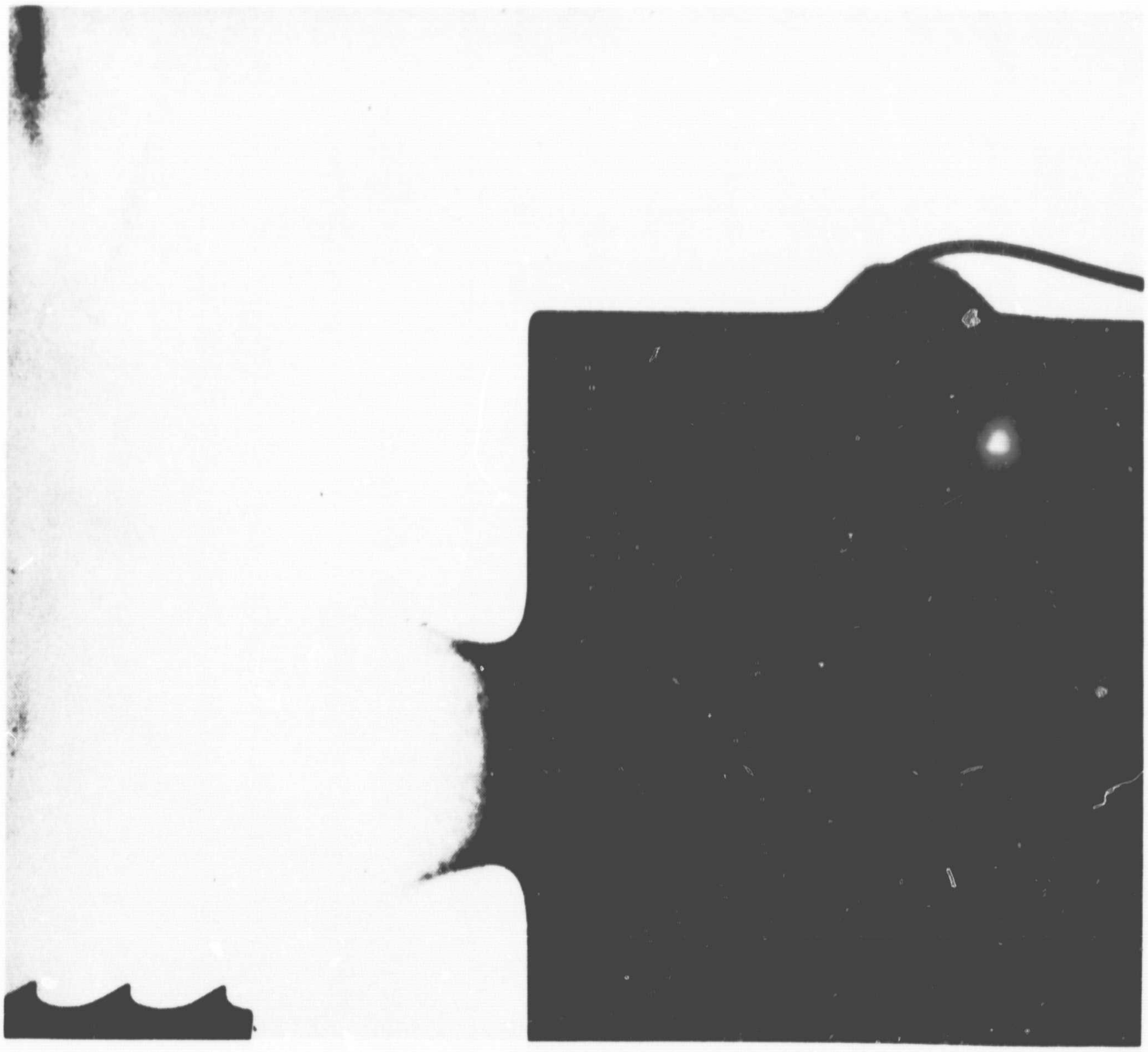

FIGURE 18. RADIOGRAPH OF TARGET EJECTA 7.3 μsec AFTER IMPACT (SHOT 395-16)

Figure 19 presents a similar view taken 13.6 μsec after impact on Shot 395-17. The purpose of this shot was to impact a 1.0-g sphere into a large basalt target at 6.4 km/sec. The target assembly, described previously, was designed to preserve the cratered basalt target. Figure 20 shows the resulting crater in the basalt slab. The volume of the crater was 92 ± 4 cm^3. The impact velocity was 6.4 ± 0.1 km/sec, and the kinetic energy was 2.05 x 10^{11} ergs. A plaster cast of the crater was sectioned along both a horizontal and vertical plane through the center of the crater. The profiles traced from these sections are presented in Figure 21. There is no reason for the asymmetry occurring in the vertical cross section. As can be seen in Figure 18, a large piece of the surface was partially separated, but not free, from the basalt slab. Had this piece come loose, the volume of the crater would be greater and the symmetry more complete.

Figure 22 shows the damaged crater from Shot 395-18, the impact of a 1.6-g right-circular cylinder at 11.6 km/sec. The volume of this crater was measured by symmetrically simulating the missing outer diameter in the damaged quadrant, covering the shell of the crater with a thin sheet of Mylar, and filling with water. The volume was measured to be 670 ± 5 cm^3; however, because of the damaged condition of the target an accuracy of ± 20% would be reasonable. The kinetic energy of the projectile can be estimated at 1.1 x 10^{12} ergs, assuming a 20% mass loss to erosion during the launch cycle. Because of the lost diagnostics it is not possible to assign a meaningful error limit to the impacting energy. Figure 23 shows a cross section of the crater. The depth and diameter of the crater were 4.7 and 23 cm respectively.

FIGURE 19. RADIOGRAPH OF TARGET EJECTA 13.6 μsec AFTER IMPACT (SHOT 395-17)

FIGURE 20. BASALT CRATER FORMED BY IMPACT OF 1.0-g SPHERE AT 6.4 km/sec

6692

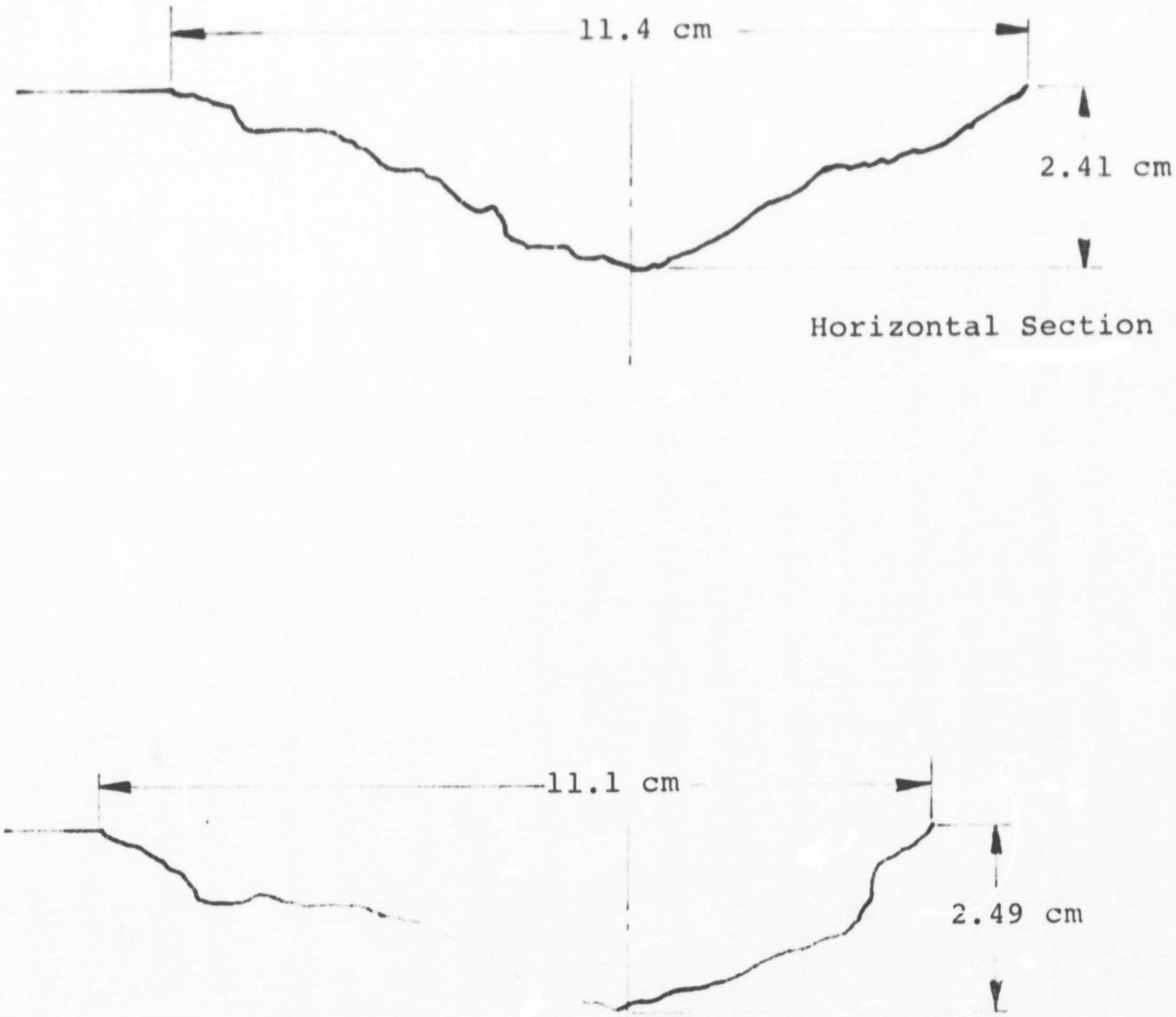

FIGURE 21. PROFILES OF CRATER FORMED BY IMPACT OF 1.0-g SPHERE AT 6.4 km/sec

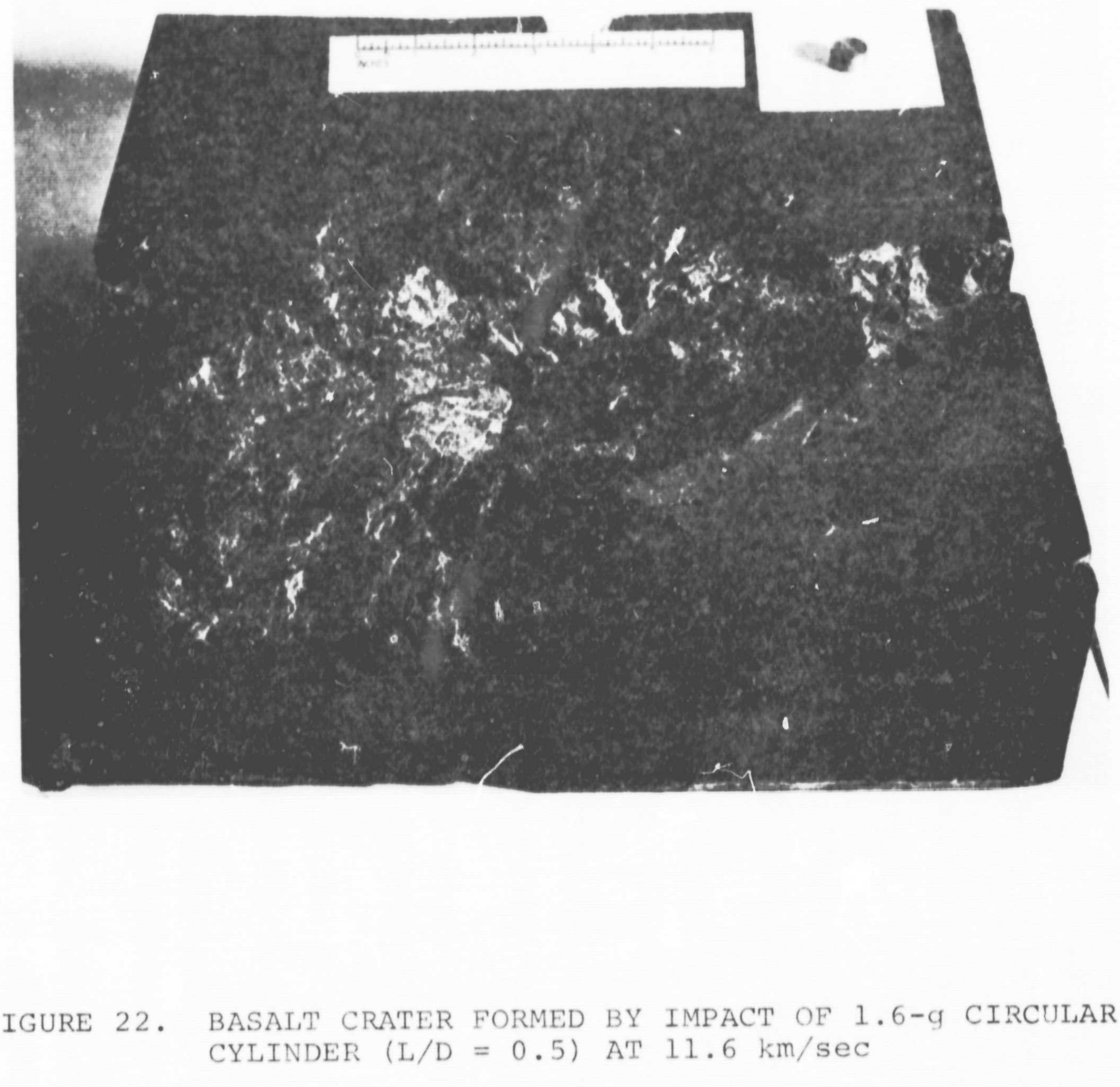

FIGURE 22. BASALT CRATER FORMED BY IMPACT OF 1.6-g CIRCULAR CYLINDER (L/D = 0.5) AT 11.6 km/sec

6693

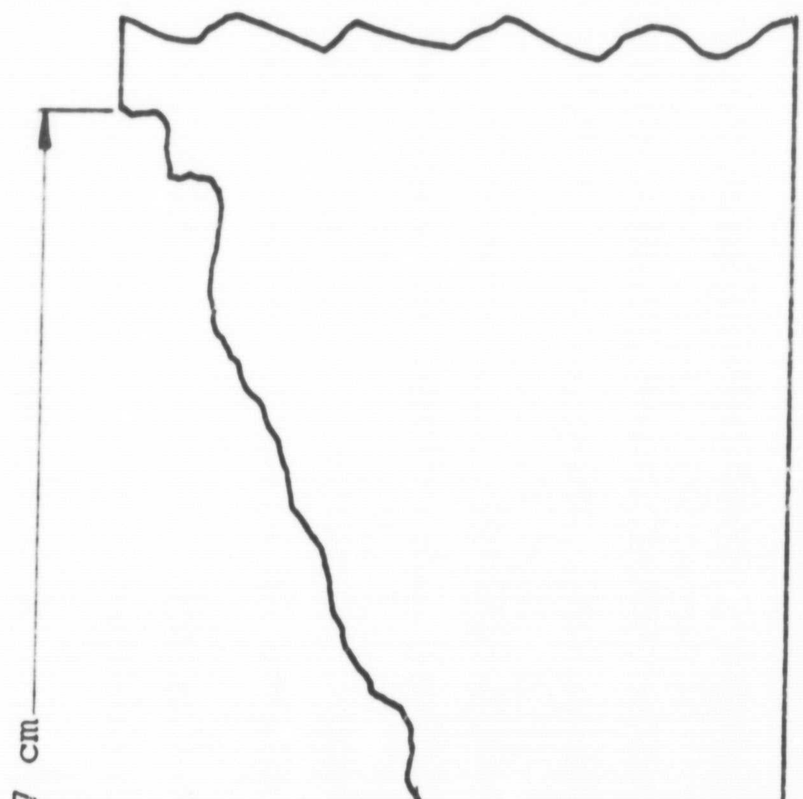

FIGURE 23. CROSS SECTION OF CRATER FORMED BY IMPACT OF 1.6-g CIRCULAR CYLINDER (L/D = 0.5) AT 11.6 km/sec

Moore, Gault, and Heitowit (Reference 24) have presented impact cratering data for basalt indicating that the mass of target ejecta per unit of projectile energy is an increasing function of projectile energy. These data, along with those obtained from the present program, are shown in Figure 24. A least-squares fit to the data of Moore et al., indicated the following relationship:

$$M_e = 10^{-10.613} \left[\left(\frac{\rho_p}{\rho_t} \right)^{1/2} E_p \right]^{1.189} \qquad (1)$$

where M_e = ejected mass (grams)

E_p = projectile energy (ergs)

ρ_p = projectile density

ρ_t = target density

The square root of the density ratio of projectile-to-target density is a normalization factor that facilitates the comparison of craters formed by projectiles of different densities. The exponent of the normalized energy term

$$\left[\left(\frac{\rho_p}{\rho_t} \right)^{1/2} E_p \right]$$

differs significantly from 1.000, a fact noted in Reference 24 as being consistent with a decrease of the effective target strength of basalt with increasing size of the resulting crater.

The ejecta mass of the two craters reported in the present program are plotted in Figure 24. The mass of target ejecta was determined by multiplying the measured crater volume by the target density. The two points although somewhat below the data of Moore et al, are consistent with empirical relationship of Equation (1), and provide confirmation of the effective target strength theory.

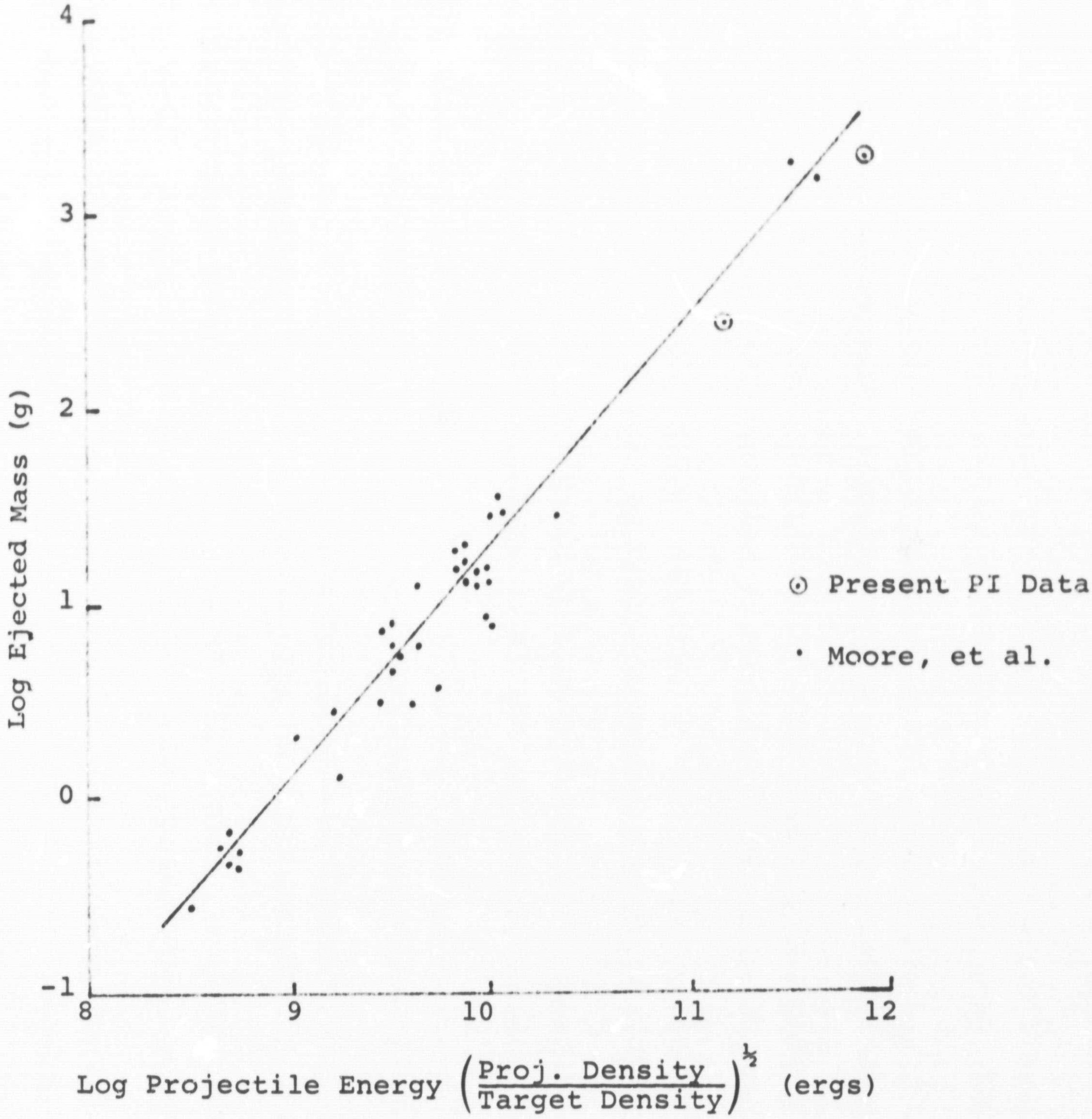

FIGURE 24. EXPERIMENTAL RELATIONSHIP BETWEEN EJECTED MASS AND PROJECTILE PROPERTIES FOR IMPACT CRATERS IN BASALT

SECTION VII

SUMMARY

A program has been instituted, under Contract No. NAS 9-8031 for the National Aeronautics and Space Administration, that has as its goal the correlation of the size and morphology of lunar surface craters with the mass and velocity of an impacting meteroid. In this first phase of the program a series of hypervelocity impact tests were performed, and static and dynamic material behavior tests were carried out and used as the basis for an analytic model describing basalt.

The propagation of spherically diverging shock waves has been studied experimentally in basalt and a mathematical model incorporating material properties has been constructed to describe this propagation. An irreversible phase transition by the constitutive minerals of basalt played an important role in the material behavior. The model used to fit the data had a constant yield strength of 1.0 kbar.

An explosively driven light-gas gun was used to launch 1.0-g spheres to a speed of 6.4 km/sec and impact against basalt targets. Basalt was selected for this study because of its apparent likeness to lunar rock. Some of the basalt targets were instrumented with embedded piezoresistive manganin gauges that monitored stress-time profiles at various depths within the target. Other targets were composed of massive assemblies designed to allow complete crater formation to occur without the influence of edge reflections. The crater formed by a 1.0-g sphere traveling at 6.4 km/sec (projectile energy of 2.05×10^{11} ergs) had a volume of 92 cm^3 and a depth of 2.5 cm. From the observed peak stress attenuation data, the peak stress at a depth of 2.5 cm was found to be approximately 0.060 Mbar. This is roughly the same stress level at which a phase transition occurs in basalt.

A modified launcher was used to fire a 2-g cylindrical projectile against a basalt target at 11.6 km/sec. Although the integrity of the projectile at impact was not verified and the target was subjected to nonimpact induced damage, it was still possible to investigate the crater. The volume of the crater was estimated to be 670 cm^3, while the projectile energy at impact was estimated to be 1.21×10^{12} ergs. Within the accuracy of the experiment the resulting two data points confirm the empirical ejecta mass-projectile energy curve determined by Moore, Gault, and Heitowit for basalt.

The next step toward attaining the goal of this overall program would be to attempt an analytic simulation of a hypervelocity impact into basalt. The successful simulation of the laboratory impact experiment will lend confidence to the analytic simulation of a more realistic lunar cratering problem.

REFERENCES

1. D. E. Gault, W. L. Quaide, and V. R. Oberbeck, "Interpreting Ranger Photographs from Impact Cratering Studies," The Nature of the Lunar Surface, W. N. Hess, et al. (eds.), (Johns Hopkins Press, Baltimore, Maryland, 1966a), Chapter 6.

2. L. D. Jaffe, et al., "Principal Results from Surveyor 5," J. Geophys. Res. 73, 22, 7165 (1968).

3. L. D. Jaffe, "Surveyor 6 Lunar Mission," J. Geophys. Res. 73, 16, 5297 (1968).

4. V. R. Oberbeck and W. L. Quaide, "Estimated Thickness of a Fragmental Surface Layer of Oceanus Procellarum," J. Geophys. Res., 72, 18, 4697 (1967).

5. W. L. Quaide and V. R. Oberbeck, "Thickness Determination of the Lunar Surface Layer from Lunar Impact Craters," J. Geophys. Res. 73, 16, 5247 (1968).

6. H. F. Waldron, E. T. Moore, Jr., G. B. Steel, and C. S. Godfrey, "A Mechanism for the Conversion of the Chemical Energy of Explosive to the Kinetic and Internal Energy of a Gas," AIAA Paper No. 67-178, presented at the AIAA Fifth Aerospace Sciences Meeting, New York, New York (January 1967).

7. E. T. Moore, Jr., H. F. Waldron, and C. S. Godfrey, "Recent Developments in the Use of Chemical Explosives for Hypervelocity Test Devices," Proc. of the Fifth Hypervelocity Techniques Symposium, Vol. II, Denver, Colorado (March 1967).

8. J. D. Watson, E. T. Moore, Jr., D. Mumma, and J. S. Marshall, "Explosively Driven Light Gas Guns," PIFR-024/065, Physics International Company, San Leandro, California (September 1967).

9. V. G. Gregson, T. J. Ahrens, and C. F. Petersen, "Dynamic Properties of Rocks," AFCRL-63-662, Stanford Research Institute, Menlo Park, California (1963).

10. A. H. Jones, W. M. Isbell, F. H. Shipman, R. D. Perkins, S. J. Green, and C. J. Maiden, "Material Properties Measurements for Selected Materials," MSL-68-9, General Motors Technical Center, Warren, Michigan (1968).

REFERENCES (cont.)

11. M. L. Wilkins, B. Squier, and B. Halperin, "The Equation of State for the Detonation Products of PBX 9404 and LX04-01," UCRL-7797, University of California Lawrence Radiation Laboratory, Livermore, California (April 1964).

12. D. Bernstein and D. D. Keough, "Piezoresistivity of Manganin," J. Appl. Phys. 35, 1471 (May 1964).

13. D. D. Keough, R. F. Williams, and D. Bernstein, "Piezoresistive Pressure Transducer," 64-WA/PT-5, presented at the Winter Annual Meeting of the American Society of Mechanical Engineers, New York, (November 29-December 4, 1964).

14. A. Klein and W. Shimmin, "Pressure Transducer Research," AFWL-TR-67-80, Physics International Company, San Leandro, California (1967).

15. C. Wang, "Phase Transition in Rocks Under Shock Compression," Earth Planetary Sci. Letters 2, 107-113 (1967).

16. J. T. Rosenberg, T. J. Ahrens, and C. F. Petersen, "Dynamic Properties of Rocks," DASA-2112, Stanford Research Institute, Menlo Park, California (1968).

17. M. W. McKay and C. S. Godfrey, "Study of Spherically Diverging Shock Waves in Earth Media," PIFR-064, Physics International Company, San Leandro, California (March 1969).

18. C. G. Balmer (compiler), "Physical Properties of Some Typical Foundation Rocks," Concrete Laboratory Report No. SP-39, U. S. Bureau of Reclamation, Denver, Colorado (1953).

19. J. Handin (compiler), in Handbook of Physical Constants, S. P. Clark, Jr. (ed), Geological Society of America, Memoir 97 (1966).

20. D. Griggs, F. Turner, and H. C. Heard, Rock Deformation, Geological Society of America, Memoir 79 (1960).

21. J. D. Watson and C. S. Godfrey, "An Investigation of Projectile Integrity Using Computer Techniques," Proc. of Fifth Hypervelocity Techniques Symposium, Vol. II, Denver, Colorado March 1967).

REFERENCES (cont.)

22. D. E. Maxwell, R. Hofmann, D. J. Andrews, and E. T. Trigg, "Study of Two-Dimensional Calculation of Cratering," PIFR-032, Physics International Company, San Leandro, California (June 1966).

23. J. W. Gehring, C. L. Meyers, and J. A. Charest, "Experimental Studies of Impact Phenomena and Correlation with Theoretical Models," TR-64-66, General Motors Defense Laboratories, Goleta, California (December 1964).

24. H. J. Moore, D. E. Gault, and E. D. Heitowit, "Change of Effective Target Strength with Increasing Size of Hypervelocity Impact Craters," Proc. of Seventh Hypervelocity Impact Symposium, Vol. IV, Tampa, Florida (November 1964).